Isomer Differentiation of Trapped C16H10+ Using Low-Energy Collisions and Visible/VUV Photons

M. Viswanathan Vinitha, Venkateswara Rao Mundlapati, Alexandre Marciniak, Mickaël Carlos, Hassan Sabbah, Anthony Bonnamy, Loïc Noguès, David Murat, Odile Coeur-Joly, Christine Joblin

Isomer Differentiation of Trapped $C_{16}H_{10}^+$ Using Low-Energy Collisions and Visible/VUV Photons

M. Viswanathan Vinitha,[†,¶] Venkateswara Rao Mundlapati,[†,¶] Alexandre Marciniak,[†,‡,¶] Mickaël Carlos,[†] Hassan Sabbah,[†] Anthony Bonnamy,[†] Loïc Noguès,[†] David Murat,[†] Odile Coeur-Joly,[†] and Christine Joblin[*,†]

†*Institut de Recherche en Astrophysique et Planétologie (IRAP), Université Toulouse III - Paul Sabatier, CNRS, CNES, 9 Avenue du Colonel Roche, F-31028 Toulouse, France*
‡*Current address: Laboratoire Collisions Agrégats Réactivité (LCAR/IRSAMC), Université Toulouse III - Paul Sabatier, CNRS, 118 Route de Narbonne, F-31062 Toulouse, France*
¶*These authors have equally contributed*

E-mail: christine.joblin@irap.omp.eu
Phone: +33 (0)5 61 55 86 01

Abstract

Polycyclic aromatic hydrocarbons are major species in astrophysical environments and this motivates their study in samples of astrochemical interest such as meteorites and laboratory analogues of stardust. Molecular analysis of carbonaceous matter in these samples show a dominant peak at m/z = 202.078 corresponding to $C_{16}H_{10}$. Obtaining information on the associated isomeric structures is a challenge for the molecular analysis of samples available in very small quantities (mg or less). Here we show that coupling laser desorption ionization mass spectrometry with ion trapping opens up the possibility of unraveling isomers by activating ion fragmentation via collisions or photon absorption. We report the best criteria for differentiating isomers with comparable dissociation energies, namely pyrene, fluoranthene, and 9-ethynylphenanthrene, on the basis of the parent dissociation curve and the ratio of dehydrogenation channels. Photoabsorption schemes (multiple photon absorption in the visible range and single photon absorption at 10.5 eV) are more effective in differentiating these isomers than activation by low energy collisions. The impact of the activation scheme on the fragmentation kinetics and dehydrogenation pathways is discussed. By analyzing the 10.5 eV photodissociation measurements with a simple kinetic model, we were able to derive a branching ratio for the H and $2H/H_2$ loss channels of the parent ions. The results suggest a role in the formation of H_2 for bay hydrogens that are present in both fluoranthene and 9-ethynylphenanthrene. In addition, we suggest for the latter the presence of a highly competitive 2H loss channel, possibly associated with the formation of a pentagonal ring.

Introduction

Molecular mass spectrometry analysis revealed that various carbonaceous samples contain a dominant peak at m/z = 202.078 corresponding to a polycyclic aromatic hydrocarbon (PAH) of formula $C_{16}H_{10}$. These samples include soot particles generated in flames,[1] diesel fuels and particulate matter,[2] cosmic dust analogues,[3,4] and carbonaceous chondrite meteorites.[5–8] Shukla and Koshi[9] showed that in combustion reactions, different chemical pathways lead to the preferential formation of

pyrene or fluoranthene. Each isomer could then lead to different species by subsequent growth. Fluoranthene could lead to fullerene-like structures due to the presence of the pentagonal ring which allows the formation of 3D structures. On the other hand, from pyrene, growth processes by the hydrogen abstraction/vinylacetylene addition mechanism, can lead by systematic ring expansions to more complex PAHs and finally to 2D graphene-like structures.[10] Therefore, identifying the dominant isomeric structure in a given sample could provide clues to its chemical history. The key role of medium-sized PAHs, particularly pyrene, in soot nucleation is also a much debated topic.[11–15].

A robust mass spectrometry (MS) method for differentiating isomers is to separate them by their affinity with a given medium. This is the basis of chromatography, which is a powerful method in chemical analysis and identification of isomeric structures. Using a gas chromatograph-mass spectrometer (GC-MS), Basile et al.[5] detected more than thirty PAHs in solvent extracts from the Murchison meteorite, with fluoranthene and pyrene constituting 58% of the PAHs detected in relative concentration, with both isomers having comparable abundances. Using a similar technique, Naraoka et al.[6] studied the molecular composition and carbon isotopic abundances of PAHs in an Antarctic carbonaceous chondrite. They identified more than 70 PAHs, fluoranthene and pyrene being the most abundant. They proposed two chemical pathways to explain the formation of these PAHs and called them the pyrene series and the fluoranthene series.

GC-MS analysis requires a sufficient amount of sample and involves different preparation steps for the extraction of species of interest, including the use of solvents. It may therefore not be suitable for *in situ* analysis in chemical reactors and for molecular analysis of complex and rare samples, as we will see later. In the field of combustion chemistry, a number of techniques have been interfaced with reactors for on-line analysis, such as resonance enhanced multiphoton ionization (REMPI)[16–19]. The potential of studies using tunable VUV synchrotron radiation was then demonstrated, including photoionization mass spectrometry[20–22] and photoelectron coincidence spectroscopy[23,24], with the latter technique offering the best potential for isomer differentiation, as also demonstrated in other studies.[25,26]

Regarding the analysis of molecular complexity in dust samples that are precious[27] and/or heterogeneous.[1,28], laser desorption ionization mass spectrometry (LDI-MS) has proven to be an interesting method. The technique has been applied to soot samples.[1,29] Recent work in our group has demonstrated the very high sensitivity (attomole level) of the two-step LDI-MS to follow molecular families of PAHs, carbon clusters, hydrogenated carbon clusters, and fullerenes. We have applied this technique to the analysis of laboratory analogues of stardust[4,30,31] and of meteorite samples.[8,29,32,33] An originality of our setup is to be equipped with an ion trap so that ions can be activated by collisions or by absorption of photons and their dissociation features used to obtain information on the structure of the ions.

McLuckey and Goeringer[34] have reviewed methods for slow heating activation of ions, with collision-induced dissociation (CID) being the one commonly implemented in ion trapping instruments. Concerning PAHs, such experiments revealed notable differences between isomers regarding their dehydrogenation pathways.[35–37] Among photon activation methods, infrared multiple photonic dissociation spectroscopy (IRMPD) has been most widely used to characterize PAH cations and identify their fragments by taking advantage of the free electron laser for infrared experiments (FELIX).[38–44] In order to study the isomers formed during the dissociative -H ionization of methylated PAHs, an alternative technique using Ne-tagged ions produced in cryogenic traps has proven to be more appropriate.[43,44] Finally, a number of studies have explored the unimolecular dissociation of PAH cations using vacuum ultraviolet (VUV) synchrotron irradiation and photoion mass spectrometry[45,46] or the more advanced imaging photoelectron photoion coincidence spectroscopy (iPEPICO).[26,47–50] These studies concern neutrals that experience disso-

ciative ionization by absorption of a single VUV photon. Our group has studied the fragmentation (and ionization) of trapped PAH cations subjected to VUV irradiation.[51–53] This work has in particular revealed differences in the dehydrogenation characteristics (H, 2H, and H_2 losses) of two dibenzopyrene isomers.[54]

In this context, we investigate here the potential of three ion activation techniques to separate PAH isomers in ion trap experiments associated with LDI-MS measurements. These techniques include low-energy CID, multiple photon absorption in the visible range, and single VUV (10.5 eV) photon absorption. This VUV photon energy is well suited to study the dissociation of pyrene and fluoranthene cations.[26,51] It is also relevant for astrophysical implications.[53] We used both the AROMA (Astrochemistry Research of Organics with Molecular Analyzer) setup and the PIRENEA ('Piège à Ions pour la Recherche et l'Étude de Nouvelles Espèces Astrochimiques') setup[55]. AROMA is dedicated to ultra-sensitive two-step laser desorption laser ionization mass spectrometry (L2MS) analysis whereas PIRENEA is dedicated to the study of the photophysics of PAHs in conditions close to those encountered in the interstellar medium. Our focus is on $C_{16}H_{10}^+$ for which we consider three isomers, namely pyrene (Pyr^+), fluoranthene (Flu^+), and 9-ethynylphenanthrene (EtP^+) (structures in Figure 1). The CID experiments were performed on AROMA, while the photoexcitation schemes involving either visible or VUV photons were performed with PIRENEA. After a description of the experimental methods, we present the results obtained for the three types of experiments. Two criteria are used for the differentiation of the isomers, namely the parent dissociation curve/yield and the ratio between the -2H/H_2 and -H channel intensities. We discuss the potential of each of the three methods for isomer discrimination. Further analysis of the data is performed by a simplified kinetic Monte Carlo model for the CID experiments and a kinetic analysis for the photoexcitation experiments. This allows us to provide additional information on the stability and dissociation pathways of the different species under the studied excitation conditions.

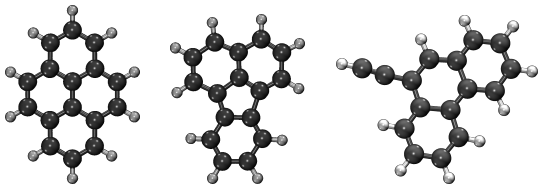

(a) (b) (c)

Figure 1: Molecular structures of the studied $C_{16}H_{10}^+$ isomers, optimized with the GAUSSIAN16 package at the B3LYP/6-31g(d,p) level of theory: (a) pyrene (Pyr^+), (b) fluoranthene (Flu^+), and (c) 9-ethynylphenanthrene (EtP^+).

Methods

Cation production

The chemical samples are from Sigma-Aldrich (> 97% purity). In all experiments, the ions are produced in gas phase using well established LDI techniques. For the AROMA setup, the desorption and ionization steps are separated using two different lasers. The neutral samples in the solid phase are desorbed from the sample plate using the fundamental output of a Nd:YAG pulsed laser at 1064 nm (Q-Smart 450, Quantel). The resulting PAH plume is then ionized by the fourth harmonic of a Nd:YAG laser at 266 nm. For the PIRENEA setup, the molecules are desorbed and ionized from a solid aluminum target by using a single 266 nm pulse whose energy and focal spot are optimized for each studied species.

CID experiments with the AROMA setup

Low energy CID measurements reported in this work were performed using AROMA. The experimental setup is explained in detail elsewhere[8] and only a brief description is presented here (scheme in Figure 2). The ions generated by two-step LDI are extracted and collimated into an octupole ion guide using a set of high voltage DC lenses. The octupole transmits these ions into a segmented (q1-q8) lin-

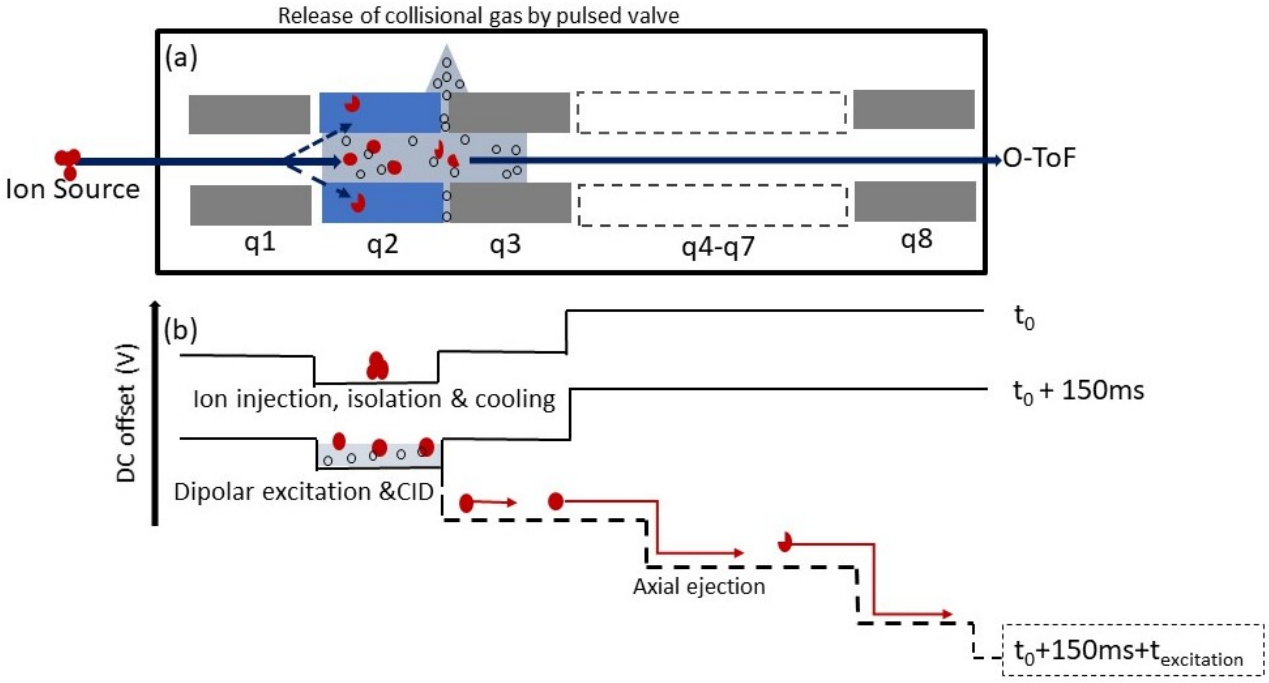

Figure 2: (a) Scheme of the CID experiment using the AROMA setup. The ionization products of each isomeric species are injected into the q2 segment of the LQIT where they are subjected to isolation, cooling and slow heating by applying a dipolar excitation in a bath of rare gas (He/Ar, black circle). This induces dissociation over time (parent and fragment are respectively represented by full and broken red disks) and ions are mass-analyzed by a high resolution orthogonal ToF (o-ToF) mass spectrometer. (b) The DC states of each segment of the LQIT are illustrated along with the time required for performing one CID cycle.

ear quadrupole ion trap (LQIT). The ions are initially trapped in the q2 segment of LQIT and cooled by pulsed injection of He buffer gas. Parent ions are further isolated in q2 through minimal ion manipulation to avoid building additional kinetic and internal energy excitation. The isolated parent ions (sometimes with residual ^{13}C isotopomers at the percentage level) are kinetically excited by applying a dipolar AC signal at a frequency close to the resonant frequency of the pure ^{12}C parent ion (f_s = 187 kHz), in the presence of a rare gas (He or Ar). Helium is injected into the LQIT and is used as a buffer gas to cool down ions in all cases, and as a collision gas in He CID experiments. When Ar is used, it is injected through another valve into the octapole ion guide. For CID, the gas is injected at a peak pressure of $\sim 10^{-3}$ mbar and the DE is applied at the resonance frequency in He and slightly off resonance in Ar. The time delay between gas injection and DE was optimized to obtain a higher fragmentation rate. The resulting dissociation products are mass-analyzed by a high resolution (m/$\Delta m \sim 10^4$) orthogonal time-of-flight (o-ToF) mass analyzer. The CID measurements are repeated by varying the duration of the DE. The carbon loss channels are found to be minor (see calibration experiment reported in Figure S1(b)), in line with previous CID measurements.[26] Recording these channels requires additional measurements in which the delay time between the LQIT exit and the o-ToF extraction pulse is changed. We therefore decided to neglect these channels.

Photodissociation experiments with the PIRENEA setup

Photoactivation of $C_{16}H_{10}^+$ isomers was performed using PIRENEA,[55] a cryogenic ion cyclotron resonance (ICR) trap capable of Fourier

transform mass spectrometry (FT-ICR-MS). It is especially designed to study the photophysics[53,56] of PAH cations in physical conditions that approach those of the interstellar medium (~ 30 K and $\sim 10^{-11}$ mbar). The setup scheme and a measurement timing chart are depicted in Figure 3(a)-(b) and further details can be found in Ref. 53. The PAH cations produced by LDI can be stored over long timescales (hundreds of seconds) into the cryogenic ICR cell. Excitation into cyclotron motion is used to perform FT-ICR-MS[57] or to eject unwanted species, such as isotopomers or fragments generated by the ion production. Pure $^{12}C_{16}H_{10}^{+}$ species can therefore be isolated. They are exposed for a couple of seconds to $\sim 10^{-8}$ mbar of He buffer gas to improve their cooling.

The prepared ions are then photoprocessed during the irradiation time, t_{irr}, by ns laser pulses coming either from a tunable Visible optical parametric oscillator (Vis-OPO, Laser 1) or from a 10.5 eV VUV source (Laser 2). Laser 1 has a duration of 5 ns and it is collimated on a typical spot size of 2.4×10^{-1} cm^2 which, for a 4 mJ pulse, corresponds to a fluence of 16.6 mJ cm^{-2} and a photon flux of 7.3×10^{24} photons s^{-1} cm^{-2} at 436 nm. The design of Laser 2 is based on a Xe:Ar tripling cell seeded by a 355 nm laser (3rd harmonic of the Nd:YAG laser) that is partially converted (conversion rate of 10^{-6}) into a VUV photon beam at 118 nm (10.5 eV) with a flux of $\sim 10^{13}$ photons s^{-1} cm^{-2}. More information on the VUV source is available in Marciniak et al.[53].

The laser sources are operated at 10 Hz (100 ms between each pulse) and the laser beam position has been optimized to overlap the ion cloud along the horizontal axis of the ICR cell. In the case of the OPO experiments, a flux of 7.3×10^{24} photons s^{-1} cm^{-2} at 436 nm corresponds to a regime where an average of two or more photons are absorbed per pulse by the pyrene cation.[58] For a single pulse, a number of events will thus lead to ion heating and not dissociation. Nevertheless, the accumulation of energy from pulse to pulse will lead to a contribution to the dissociation signal. To minimize this contribution, we have performed experiments in which the laser pulses are separated by a larger delay (δt_{irr}). The cooling of hot ions can take seconds or more as shown in the case of $C_{24}H_{12}^{+}$.[59] In this work, we used a value of $\delta t_{irr} = 2$ s for experiments involving delayed pulses. In the VUV measurements, such a delay is not needed because the VUV photon flux is low enough that the effective average delay between the absorption of two VUV photons is of a few hundred seconds.[53] Finally, after laser irradiation, a very high resolution mass spectrum is recorded and the ions are ejected before an entire new sequence. Using PIRENEA, we have studied the $C_{16}H_{10}^{+}$ isomers by acquiring (i) their action spectra in the range 410 nm to 480 nm, (ii) their breakdown curves as a function of the pulse energy or the number of pulses at two specific wavelengths, and (iii) their breakdown curves as a function of the VUV irradiation time.

Data analysis

Only singly charged ions were observed in the reported experiments. We therefore associate each mass peak to a mass M_i and define its normalized intensity by:

$$I_{M_i}^{\text{norm.}} = \frac{I_{M_i}}{\sum_{M_j} I_{M_j}} \quad (1)$$

In the following of the article, we notably report breakdown curves, which display the variation of the normalized intensity of the parent cations ($C_{16}H_{10}^{+}$) as a function of the collisional excitation or the irradiation time. For sake of simplicity, we name it I_{202}. We repeated each measurement until we obtained reasonable error bars as illustrated by the results displayed all along this article. In this study, we also present the intensity ratio corresponding to the $2H/H_2$ over H loss channels ($R_{200/201}$):

$$R_{200/201} = \frac{I_{200}^{\text{norm.}}}{I_{201}^{\text{norm.}}} \quad (2)$$

In this case, the error bar is computed by :

$$err\left(R_{200/201}\right) = \frac{\Delta I_{200}}{I_{201}} + \frac{\Delta I_{201}}{I_{201}} R_{200/201} \quad (3)$$

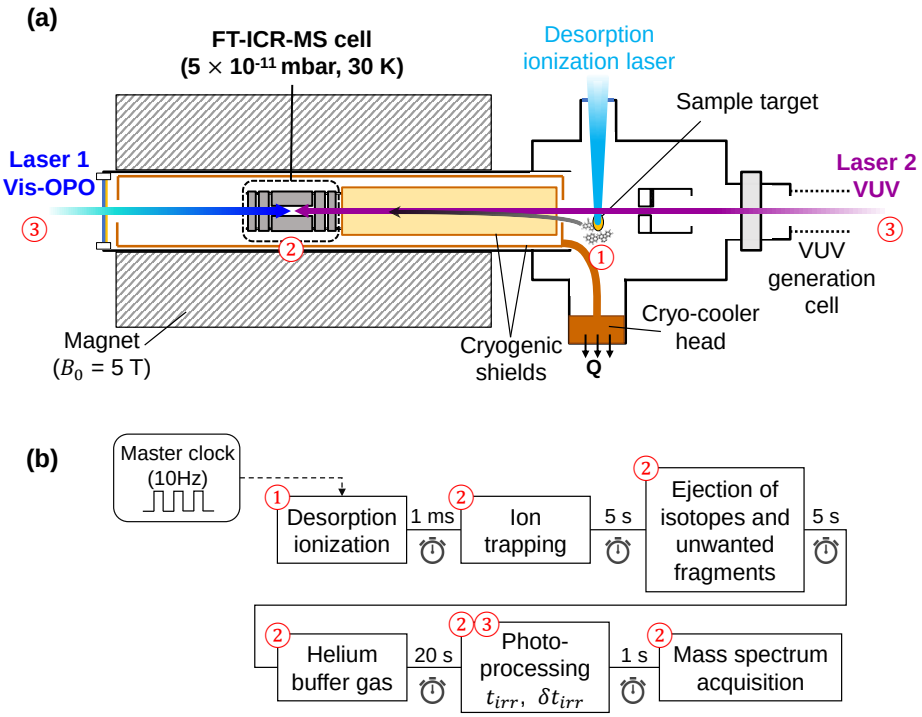

Figure 3: (a) Scheme of the PIRENEA setup coupled to a Vis-OPO (Laser 1) and a 10.5 eV VUV source (Laser 2). Cationic species are produced in the gas phase by LDI of a sample target with a 266 nm-laser and are stored in the cryogenic ICR cell. After the laser interaction, the ions are analyzed in mass by FT-ICR-MS at very high resolution. (b) Time diagram of a PIRENEA measurement sequence. The numbers circled in red link each step to its location in the setup.

where ΔI_{M_i} corresponds to the standard deviation of $I_{M_i}^{\text{norm.}}$ for a given series of measurements.

Model for CID experiments

A simple model was constructed to simulate the dissociation kinetics in the multiple collision environment of the AROMA linear ion trap. Ion kinematics were modeled using Simion© software within a hard sphere model to describe the collisions of the ions with the buffer gas. The simulation begins by assuming that the ions are thermalized at room temperature and subjected to dipolar excitation in the presence of a buffer noble gas (He/Ar) for a given time. This allows us to recover the distribution of collision energies in the center-of-mass frame, E_{com}, and the distribution of the time interval between two collisions, t_{coll} (see Figure S4).

The evolution of the internal energy distribution (IED) of the ions, during collisional activation, is modeled by performing Monte Carlo simulations in which the collision is considered as an event that can occur at a time t_{coll} and an energy E_{com} both randomly drawn from the previously calculated distributions. The transfer of kinetic to internal energy in each collision is described by $\Delta U = \eta E_{com}$, where the conversion factor η represents the mean value of collisional internal energy transfer (IET) in an inelastic collision.[60] As discussed in this review article by Drahos and Vékey[60], the details of the collisional IET distribution, which depends on collision characteristics such as the partners and the geometry of the collision, have only been studied in a limited number of cases (e.g. Ref[61]). For simplicity, we consider η to be a free parameter in our model. However, it is not fixed as a constant value over the excitation time since the internal energy of the ions evolves with time, which is expected to affect the IET distribution.[60–62] During the simulation, the internal energy for each ion is built by a succession of collisions leading to a total energy of $U = \Sigma\Delta U^i$ where ΔU^i is the increase of internal energy at the i^{th} collision. The compe-

tition between heating by collisions and dissociation is treated by comparing the inverse of the collision time ($k_{coll} = 1/\mathrm{t_{coll}}$) with the dissociation rate, $k_{diss}(U)$ as given in West et al.[26]. If $k_{coll} > k_{diss}(U)$, then collisional energy transfer occurs and increases the internal energy of the ion. Conversely, if $k_{coll} < k_{diss}(U)$, the ion dissociates. This study was performed for a set of 10^5 ions in order to simulate our experimental results.

Simple kinetic model

We use a simple kinetic model (see full description in Marciniak et al.[53]) to fit photodissociation curves as a function of either number of delayed Vis-OPO pulses or VUV irradiation time. In short, it consists in using a master equation (ME) whose solution has to fit the photodissociation kinetics of the parent and fragments. It reads :

$$\begin{cases} (1^{\mathrm{st}}) & \dfrac{\mathrm{d}I_{\mathrm{M_{parent}}}}{\mathrm{d}t}(t) = \\ & -\displaystyle\sum_{M_i<M_{\mathrm{parent}}} k_{\mathrm{frag}}^{M_{\mathrm{parent}}\to M_i} I_{M_{\mathrm{parent}}}(t) \\ & \vdots \\ (i^{\mathrm{th}}) & \dfrac{\mathrm{d}I_{M_i}}{\mathrm{d}t}(t) = \displaystyle\sum_{M_h>M_i} k_{\mathrm{frag}}^{M_h\to M_i} I_{M_h}(t) \\ & \\ & -\sum_{M_j<M_i} k_{\mathrm{frag}}^{M_i\to M_j} I_{M_i}(t) \end{cases} \tag{4}$$

where $I_{M_i}(t)$ is the population of the ion channel M_i as a function of the irradiation time t and $k_{\mathrm{frag}}^{M_i\to M_j}$ is the fragmentation rate from fragment M_i to fragment M_j. Each line of the ME is the time variation of a given channel at mass M_i which is equal to the sum of depopulation ($-\mathrm{k_{frag}^{M_i\to M_j}} I_{M_i}$, with $M_i > M_j$) and population ($+\mathrm{k_{frag}^{M_h\to M_i}} I_{M_h}$, with $M_h > M_i$) terms. The $\mathrm{k_{frag}}$ are free parameters in the fitting procedure. For each species, we build an initial ME using information from (i) previous studies (e.g., H- and/or 2H/H_2-loss channels involved in parent dissociation), (ii) the sequence relationship between fragment channels (e.g., $C_{16}H_8$ cannot produce $C_{16}H_9$), (iii) energetics (e.g., 3H/(H_2+H) loss is unfavorable at 10.5 eV) and (iv) careful observations of the kinetics of all ion channels (e.g., some channels are populated directly from $t_{irr.} = 0$ s while others are delayed). Then, the fitting algorithm optimizes the $\mathrm{k_{frag}^{M_i\to M_j}}$ values so that the ME solution fits the parent and fragment photodissociation curves at the same time. If the fits are not satisfactory, it means that some population/depopulation terms may be missing or unnecessary in the ME. These terms are iteratively implemented or removed until a fitting solution with minimum number of $\mathrm{k_{frag}^{M_i\to M_j}}$ parameters and best R^2 is found. Overall, this procedure allows us to draw a fragmentation map for the studied species with some details on the total fragmentation rate of each detected ion M_i ($k_{\mathrm{frag}}^{M_i}$) and the branching ratios associated with their daughter fragments ($R^{M_i\to M_j}$). These values are defined by:

$$k_{\mathrm{frag}}^{M_i} = \sum_{M_j<M_i} k_{\mathrm{frag}}^{M_i\to M_j} \quad , \quad R^{M_i\to M_j} = \frac{k_{\mathrm{frag}}^{M_i\to M_j}}{k_{\mathrm{frag}}^{M_i}} \tag{5}$$

where M_j are the daughter fragments of M_i.

Results

CID: experimental results

In CID experiments, the H loss channels constitute the major fragmentation channel for all the isomers. As an example, the mass spectrum of Pyr^+ obtained following CID in He is displayed in Figure S1(b). The parent ion breakdown (or depopulation) curves are presented in Figures 4(a) and (c) for CID in He and Ar, respectively. The dissociation threshold is observed to arise after about 3.5 and 0.5 ms of DE for CID in He and Ar, respectively. For CID in He, the parent breakdown curves are relatively similar for the three isomers with a tendency for Flu^+ to be less stable (Figure 4(a)). This trend is amplified in Ar gas (Figure 4(c)) with a more pronounced separation between the isomers showing that Flu^+ has the fastest dissociation kinetics followed by Pyr^+, while EtP^+ is found to have the slowest kinetics under these conditions. The fragment kinetics in He gas (see Figure S2) clearly

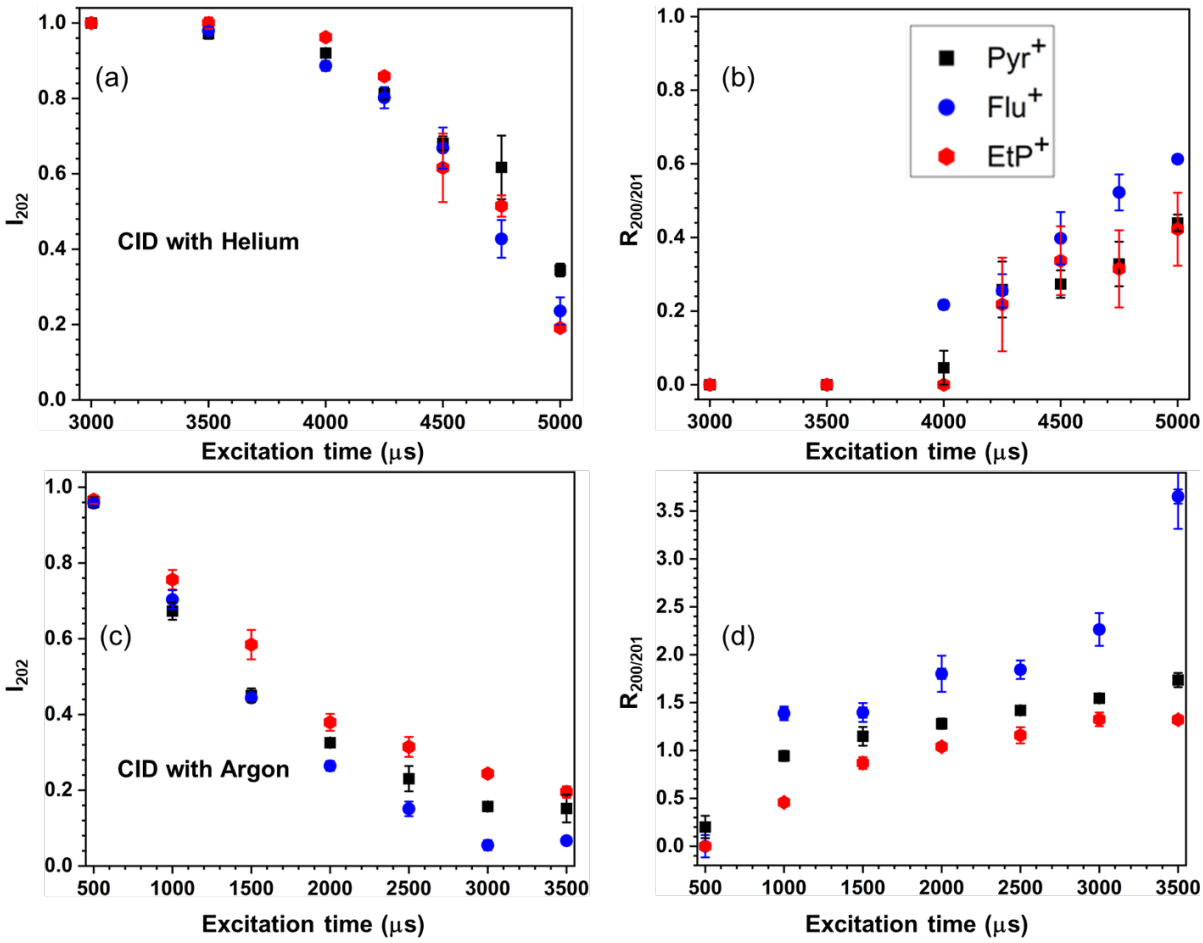

Figure 4: CID experiments (a)-(b) in He gas and (c)-(d) in Ar gas. The parent breakdown curve I_{202} and the associated fragment ratio $R_{200/201}$ are plotted as a function of dipolar excitation time. Results for the three isomers Pyr^+, Flu^+, and EtP^+ are shown with different symbols and colors. Note that, for CID in Ar, the data points at longer excitation times (e.g., 3.5 ms) should be at lower values if the carbon loss channels were considered (not measured here), however this effect does not change the conclusions we draw from these results.

shows that H-loss is the dominant fragmentation channel. The fragment corresponding to $2H/H_2$ loss appears at longer time scales, suggesting that this channel arises from the subsequent dehydrogenation of H-loss fragments after several cycles of re-excitation. This effect is found to be pronounced when the DE amplitude exceeds a certain value.[63] For CID in Ar, the dissociation kinetics is faster and the shift in time between the H and the 2H loss fragments is more difficult to estimate (see Figure S3).

The kinetics of $2H/H_2$ loss can be further characterized by $R_{200/201}$ (eq. 2). This ratio increases as a function of the excitation time for all the isomers (Figures 4 (b) and (d)). For CID in He, the signal associated with the $C_{16}H_8^+$ fragment appears about 1 ms after the parent dissociation threshold (see Figure S2). The corresponding value for CID in Ar is less than 0.5 ms (see Figure S3). Higher values of $R_{200/201}$ are achieved for Flu^+ compared to Pyr^+ and EtP^+. This is best observed for CID in Ar with a value of $R_{200/201}$ up to 3.65 for one point of Flu^+, whereas the values are all below 0.6 in He gas. Finally, we observed that for CID in Ar, species with a high degree of dehydrogenation, $C_{16}H_m^+$, where $m = 6, 7$, can be formed but with an abundance lower than 6% even for the longest excitation times (see Figure S1(c)).

CID: modeling results

Simulations using the CID model were run at a background pressure of 10^{-3} mbar (see section S1.2 for further details). In order to cover the full excitation time window, we performed 1000 and 250 collisions for CID in He and in Ar, respectively, on a set of 100000 ions. The first set of simulations were run for Pyr^+ with fitting of the breakdown curve as shown in Figure 5(a) for CID in Ar and Figure S5(a) for CID in He. This fitting allows us to retrieve the fitting parameter η (Figure S6) and the time evolution of the IED (Figure 5(b) and Figure S5(b), in Ar and He respectively). For both gases, the ion ensemble evolves in energy with time and the IED truncates at around 11.5 eV. The later value of energy is the dissociation limit at which the Pyr^+ ensemble starts depopulating due to dissociation. The ion ensemble reaches this limit in about 400 μs in Ar (see (Figure 5(b))) and 3.5 ms in He (see Figure S5(b)). The derived values for η (Figure S6) are found to decrease rapidly with excitation time and reach a value of 2% for both CID in He and Ar. This value is lower than the values of 10-20% reported for other types of molecules.[64,65] However, in our case, other uncertainties are included in this fitting parameter, such as the one on the pressure value. The absolute value of η must therefore be considered with caution. In addition, the decrease of η with excitation time could be related to the decrease of the pressure during the excitation time, because the value of η comes from a CID model in which the pressure is assumed to be constant. Another possibility is a decrease of η with the collisional energy and/or the internal energy of the ion, which can be rationalized with a shorter lifetime of the collision complex and thus a lower efficiency of inelasticity.[60,62]

The values of η fitted to the breakdown curve of Pyr^+ were then used in the simulations of Flu^+ and EtP^+. The unimolecular dissociation rate of Flu^+ is available[26] but that of EtP^+ is unknown. For the latter case, we therefore used the same rate as for Pyr^+ but applied a multiplication factor (< 1) to account for the fact that the dissociation kinetics of EtP^+ in CID experiments is slower than that of Pyr^+. Figure 5(a) for CID in Ar and Figure S5(a) for CID in He show that all simulated curves are in good agreement with the experimental curves, except for the parent breakdown curve of EtP^+ in He. This will be discussed in more detail in the General Discussion section.

Visible photoexcitation

Measurements of photoexcitation in the visible range are based on a multiphoton (or multiple photon) dissociation (MPD) scheme. For a given species, this consists of the absorption of several photons in a single pulse combined with a possible absorption of photons in consecutive pulses. Once the internal energy of the ions is sufficient, dissociation occurs. In our study, we have recorded the dependence of the MPD yield with the wavelength of the OPO (λ_{OPO}). We also studied the evolution of the breakdown curves with the energy of the laser pulse (E_{OPO}) in the case of a single pulse, and with the number of pulses for pulses delayed by 2 s.

MPD action spectra of the three $C_{16}H_{10}{}^+$ isomers are shown in Figure 6 for the 410-480 nm spectral range. They were obtained by recording, at each wavelength, the photodissociation yield of the parent species ($Y_D = 1 - I_{202}$) in %, after irradiation by five consecutive pulses of 2 mJ energy delayed by 100 ms. The spectra of Pyr^+ and EtP^+ show at least three bands in the scanned range, including a strong band in the 432-446 nm range. On the opposite, no strong band was found for Flu^+ although we noted an increase in Y_D at $\lambda_{OPO} < 420$ nm. This spectral analysis allows us to easily differentiate Flu^+ from the other two isomers.

Biennier et al.[66] determined that the absorption band of Pyr^+ in the gas phase is located at 436.2±0.2 nm with a bandwidth of 2.8 nm. The bands we observed in this range are much wider (e.g., $\sim$ 13 nm for Pyr^+). The band broadening occurs due to heating of the ion during the MPD process, which involves absorption of multiple photons in the same pulse or between consecutive pulses (see section "Photodissociation experiments with the PIRENEA setup"). Stockett et al.[59] have studied the increase of

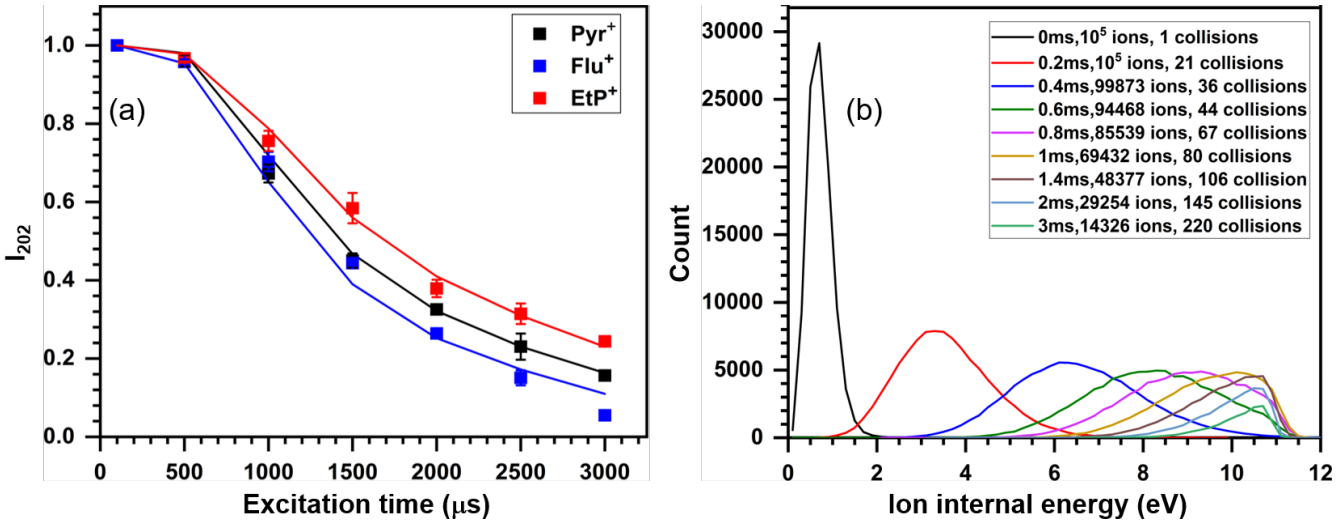

Figure 5: Model simulation results for CID in Ar. (a) Fitted breakdown curves (solid line) for the three isomeric ions. Experimental data points are shown as scattered dots. (b) Internal energy distribution of Pyr^+ as a function of the excitation time.

the bandwidth with internal energy in the case of $C_{24}H_{12}{}^+$. In addition of the temperature effect, dissociation occurs at a given threshold of internal energy which induces nonlinear saturation effects on the band profile, also leading to band broadening.

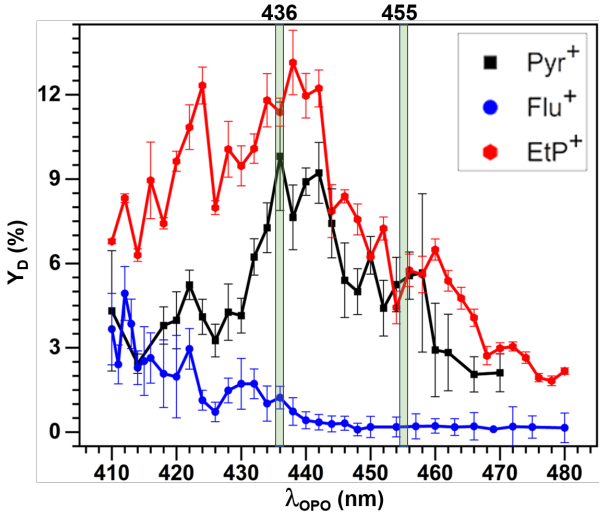

Figure 6: MPD action spectra of the $C_{16}H_{10}{}^+$ isomers. Each data point is obtained by using five consecutive laser pulses of 2 mJ. The shaded areas show the two wavelengths (436 nm and 455 nm) used for the second experiment.

In a second experiment, we recorded I_{202} and $R_{200/201}$ as a function of E_{OPO} (Figure 7). The use of a single pulse limits the excitation to absorption of multiple photons in the same laser pulse. We performed these measurements at two different wavelengths, $\lambda_{OPO} = 436$ nm and 455 nm, which correspond, respectively, to a primary and secondary absorption maximum in the MPD spectra (Figure 6). In agreement with the MPD spectra, we found that Pyr^+ and EtP^+ dissociate efficiently at $\lambda_{OPO} = 436$ nm and follow a similar breakdown curve. In contrast, Flu^+ dissociates very inefficiently (Figure 7(a)). At $\lambda_{OPO} = 455$ nm, Flu^+ remains the most inefficient to dissociate. In addition, the breakdown curves of the three isomers are well separated (Figure 7(c)). For both wavelengths, the trends observed in the parent breakdown curves are also clearly seen when the H loss or $2H/H_2$ loss fragmentation channels are considered separately (see Figure S9(a)-(d)). However, when the two channels are combined in $R_{200/201}$, this ratio increases similarly for EtP^+ and Pyr^+ (Figure 7(b),(d)). Only Flu^+ can be differentiated from the others, reaching values of 2.0 and above for the highest values of E_{OPO} (Figure 7(b),(d)). Finally, we found that the C_2H_x loss channel could be used to differentiate EtP^+ from Pyr^+ at $\lambda_{OPO} = 436$ nm but not at $\lambda_{OPO} = 455$ nm (see Figure S9(e)-(f)). However, the corresponding fragment abundances are low, typically a factor of 10 lower than the main fragment channels.

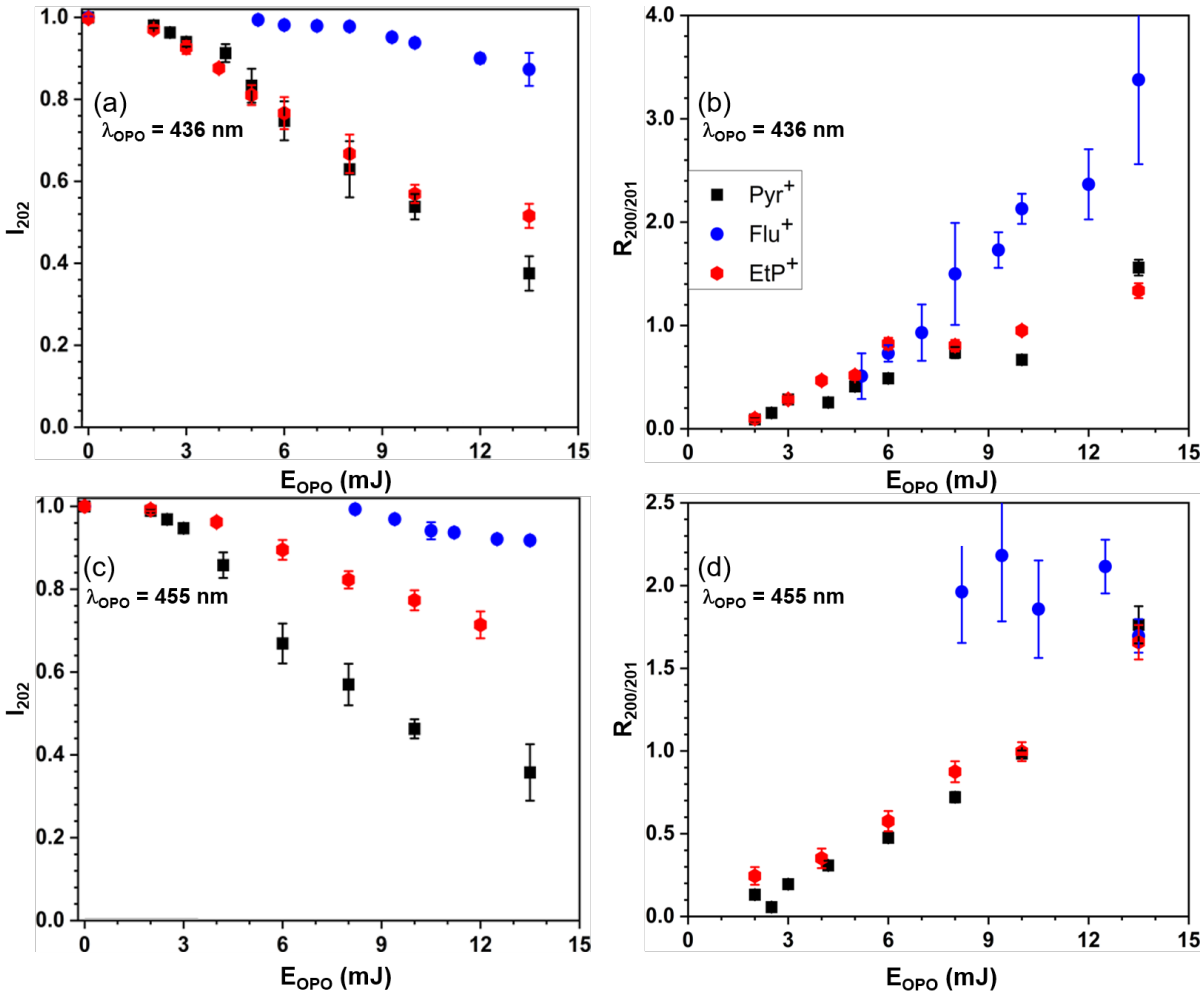

Figure 7: MPD breakdown curves of the parent ion intensity I_{202} and associated fragment ratio $R_{200/201}$ as a function of the OPO laser energy at wavelengths of (a)-(b) 436 nm and (c)-(d) 455 nm. The experiments were performed using a single pulse at each energy.

In a third experiment, we characterized the fragmentation kinetics of each isomer as a function of the number of OPO pulses. The measurements were performed at $\lambda_{OPO} = 436$ nm and for two laser energies $E_{OPO} = 4$ mJ and 14 mJ. A delay of 2 s between pulses was set to minimize the contribution of dissociation events associated with the accumulation of energy between successive pulses. The breakdown curves are presented in Figure 8 (a),(c) along with the decay curves corresponding to the fragmentation rates derived with the kinetic model described in the Methods section. At $E_{OPO} = 4$ mJ, Flu^+ shows inefficient dissociation with the increasing pulse number and its breakdown curve is well separated from the other two isomers. At $E_{OPO} = 14$ mJ the three isomers have distinct kinetics. Interestingly, the ratio of the fragmentation rates derived at the two OPO energies ($\frac{k_{frag}^{14\,mJ}}{k_{frag}^{4\,mJ}}$) is equal to ∼11 for Pyr^+ and EtP^+ while it is ∼23 for Flu^+. When related to the multiplication factor between the two OPO energies (14/4 = 3.5), these ratio values show that MPD exhibits nonlinear effects that are strongly isomer-dependent and can help differentiate these species (see also Figure S10).

Furthermore, we compare the evolution of $R_{200/201}$ as a function of the number of pulses for the three isomers in Figure 8(b),(d). At both $E_{OPO} = 4$ mJ and 14 mJ, this ratio increases with the number of pulses and no clear separation can be made between the different isomers, except at $E_{OPO} = 14$ mJ for a single pulse, where $R_{200/201}$ for Flu^+ is higher than for Pyr^+

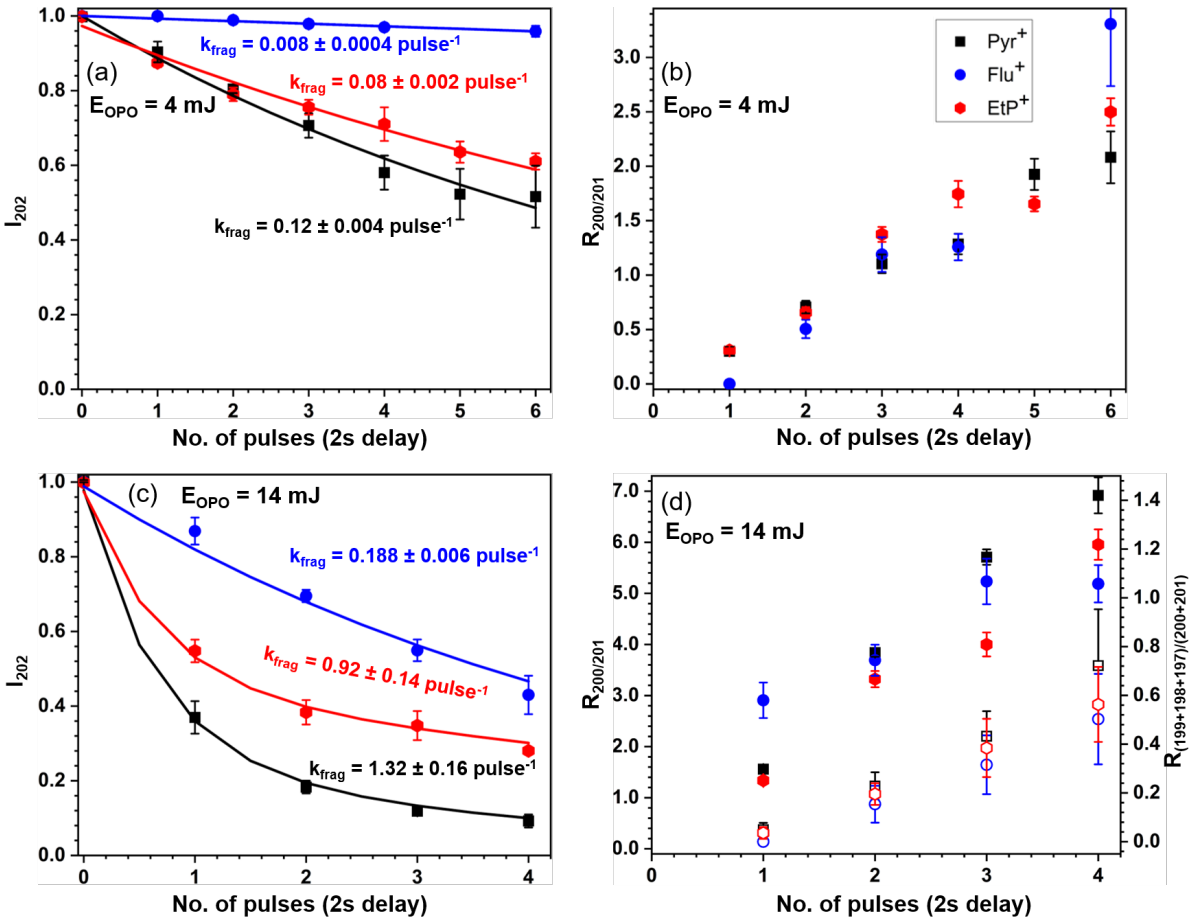

Figure 8: MPD breakdown curves of the parent ion intensity I_{202} and the associated fragment ratio $R_{200/201}$ as a function of the number of OPO laser pulses (including a 2 s delay between pulses) at $\lambda_{OPO} = 436$ nm. The laser energies used are (a)-(b) 4 mJ and (c)-(d) 14 mJ. In (d), the added empty symbols as well as the scale given on the right axis represent the fraction of the most fragmented species (i.e., the sum of the intensity of the -3H, -4H, -5H fragments relative to the sum of the intensity of the -H, -2H fragments). The solid lines and derived fragmentation rates, k, result from the fit obtained with the kinetic model described in the Methods section.

and EtP^+, similarly to what is shown in Figure 7 (b). For a larger number of pulses at $E_{OPO} = 14$ mJ, we observe that the fraction of consecutive nH loss channels (with $n \geq 3$) increases significantly and represents 50-70% relative to the fraction of main fragment channels for a number of 4 pulses (empty markers in Figure 8(d)).

We showed above that the three isomers can be differentiated in a region of relatively low absorption cross-section (e.g. $\lambda_{OPO} = 455$ nm) by recording Y_D as a function of E_{OPO}. As demonstrated now, the same can be achieved on a strong absorption peak by studying the fragmentation kinetics at high values of E_{OPO}.

VUV photoprocessing

The VUV photoprocessing measurements were performed for long irradiation times, up to 1000 s considering that the average delay between photon absorption events is on the order of a few hundred seconds (see section Methods). Note that we did not observe the formation of dication using the 10.5 eV photon source, which is in agreement with an appearance energy of Pyr^{2+} from trapped Pyr^+ of 11.7 eV[51]. By fitting the dissociation curves of the parent and fragment ions with the kinetic model (see description in the section Methods), we retrieve a fragmentation map for each isomer and extract the fragmentation rates and associated branch-

ing ratios for all ion channels involved (simplified fragmentation map in Figure 10 and full map in Figure S12).

The variation of I_{202} as a function of the VUV irradiation time is plotted in Figure 9(a) for the three isomers. Figure 9(a) also reports the curves obtained from the fits and the corresponding fragmentation rates. The results show that the kinetics of Flu^+ is well separated, with faster fragmentation ($k_{frag} = (2.8 \pm 0.2) \times 10^{-3}\,s^{-1}$), than for EtP^+ ($k_{frag} = (2.3 \pm 0.3) \times 10^{-3}\,s^{-1}$) and Pyr^+ ($k_{frag} = (1.9 \pm 0.1) \times 10^{-3}\,s^{-1}$). Although the fragmentation rates are close for the latter two isomers, the kinetic curve for EtP^+ shows a significant deviation from a single exponential depopulation behavior. It starts with a slow depopulation (in the 0-100 second range) followed by a steeper slope (in the 150-500 second range).

The values of $R_{200/201}$ are very high (~ 10) and almost constant for EtP^+ while it increases to a maximum value of $\sim$0,8 or $\sim$1,2 respectively for Pyr^+ and Flu^+ (Figure 9(b)). This shows the presence of one or more effective pathways to form $C_{16}H_8{}^+$ in EtP^+ upon absorption of a single VUV photon. Such pathways might be present in Flu^+. Indeed, if we extrapolate $R_{200/201}$ toward $t_{VUV} = 0$, we obtain a non-zero value (~ 0.3). In the case of Pyr^+, we performed a complementary experiment to check a possible contribution of a direct pathway to produce $C_{16}H_8{}^+$. A branching ratio of $\sim 2\%$ was obtained for this channel (see Figure S13), suggesting that this pathway, if present, is negligible. Otherwise, the maps for Pyr^+ and Flu^+ show a similar trend with a major H loss cascade ($M_{202} \rightarrow M_{201} \rightarrow M_{200}$) and minor C_2H_x loss channels (a few percent in both cases). On the other hand, the recovered fragmentation map for EtP^+ follows a different logic. It requires a first main isomerization step ($C_{16}H_{10}{}^{+*}$, BR $\gtrsim$,70 %) that competes with a direct $2H/H_2$ loss channel. We emphasize that without this (photo)activated isomerization step, the unusual depopulation kinetics of the parent cannot be well fitted. However, due to this extra step in the model, the fitting parameters are more interdependent, which means that the extracted values should be considered with caution (error bar of $\sim 20\,\%$, see section S2.4). The (photo)activated isomer population then leads to four fragmentation channels, namely the $2H/H_2$, H, C_2H_2, and C_4H_2 loss channels. The fragmentation maps obtained and their associated constants (rates and branching ratios) allow us to highlight major differences between EtP^+ and the other two isomers, including the opening of a direct $2H/H_2$ loss channel and the likely presence of one or several long-lived (photo)activated isomers.

Isomer differentiation

Table 1 summarizes the selected criteria, including the parent breakdown curve I_{202} as a function of the excitation condition, which is related to the dissociation yield Y_D, and the intensity ratio involving the fragment ions ($R_{200/201}$). Regarding the criterion on the parent breakdown curve, the visible MPD scheme offers the best way to differentiate the Flu^+ regardless of the laser parameter one varies: the excitation wavelength (Figure 6), the pulse energy (Figures 7 and S9), and the number of delayed pulses (Figure 8(a,c)). This is due to the much lower absorption cross section of Flu^+ compared to the other isomers in the spectral range studied from $\lambda_{OPO} \sim 432\,nm$ to $\sim 460\,nm$.[67,68]. In MPD experiments, we also found two suitable conditions for differentiation between EtP^+ and Pyr^+. Firstly, at $\lambda_{OPO} = 455\,nm$ and high values of E_{OPO}, strong nonlinear effects amplify the difference in dissociation yield between the two isomers (Figure 7). Second, by measuring the fragmentation kinetics at $\lambda_{OPO} = 436\,nm$, we found that Pyr^+ dissociates faster than EtP^+ under conditions involving delayed pulses of 2 s (Figure 8).

Regarding the fragmentation ratio given by $R_{200/201}$, we find that its value is higher for Flu^+ compared to Pyr^+ in all three types of experiments. The clearest cases are for CID in Ar for long excitation times with a value reached of $R_{200/201} = 3.65$ to be compared with a value of 1.8 for Pyr^+ (Figure 4(d)). A similar variation is observed in the MPD measurements at 436 nm for high values of E_{OPO} (Figure 7(b)).

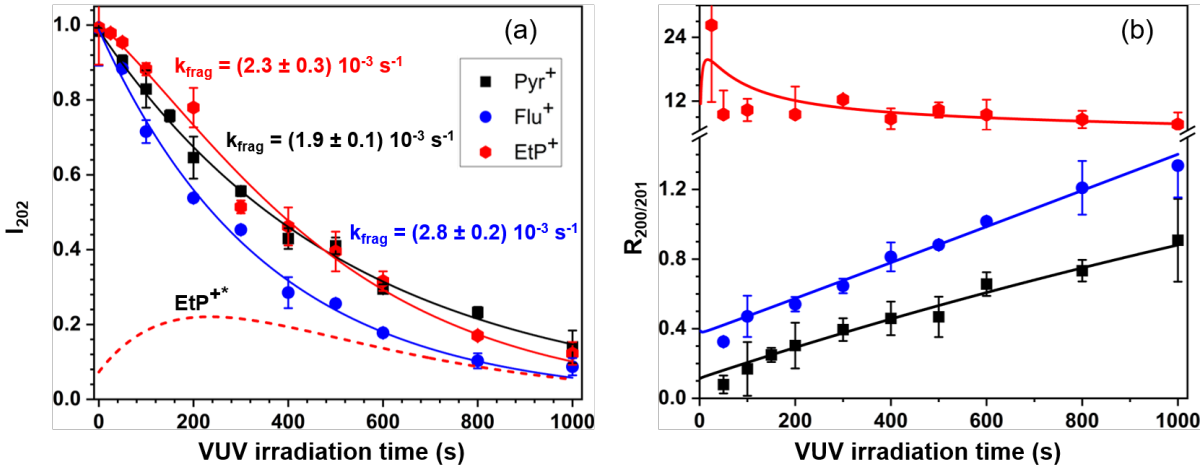

Figure 9: VUV photoprocessing of the three isomers: (a) parent breakdown curves and (b) their associated $R_{200/201}$ as a function of VUV irradiation time. The fitting curves (solid lines) and fragmentation rates (k_{frag}) were derived from the kinetic model. For EtP^+, the parent breakdown curve is different from an exponential decay. Therefore, the k_{frag} displayed is rather an effective rate which is calculated thanks to the initial population of EtP^+ parent and its isomer (the EtP^{+*} abundance is represented by the dotted curve in (a)) and their respective fragmentation rate (Figure 10(c)).

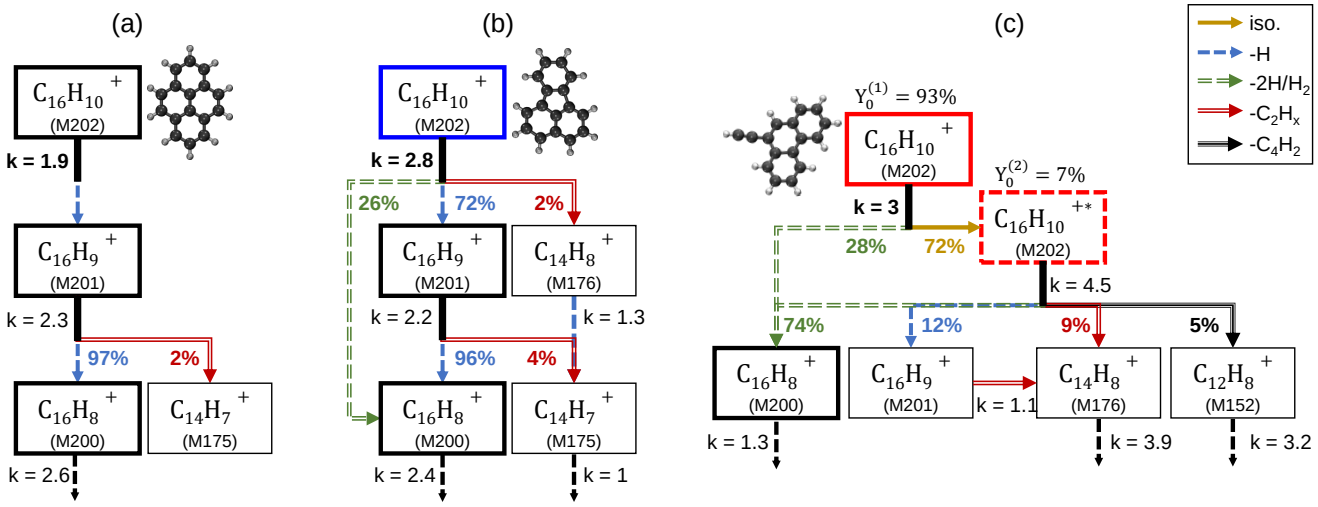

Figure 10: Simplified VUV fragmentation map of (a) Pyr^+, (b) Flu^+ and (c) EtP^+. Each arrow represents a fragment loss or a mechanism triggered by the absorption of a VUV photon (see legend). The fragmentation rate of each ion channel (written k and rounded to the first decimal) is displayed in $\times 10^{-3}$ s^{-1} and the branching ratios (rounded to integer values) are also displayed. Boxes circled in bold correspond to major ion channels ($I_{M_i}^{norm.}$ greater than 10% during the kinetics). Full maps are reported in Figure S12.

In the case of VUV photoexcitation, we note that although both Flu^+ and Pyr^+ follow a linear behavior with a similar slope, the Flu^+ ratio is well separated from that of Pyr^+ thanks to an initial offset of about 0.26, while the Pyr^+ ratio $R_{200/201}$ starts near 0. Concerning EtP^+, the VUV photoexcitation seems to be the most appropriate method to differentiate this isomer from the other two based on $R_{200/201}$. Indeed, it reaches a much higher values for EtP^+ ($\sim$ 9.6) relative to those for Flu^+ or Pyr^+ which remain below 1.5. (Figure 9(b)). In the other types of experiments, the value of $R_{200/201}$ for EtP^+ follows that for Pyr^+.

In summary, we found that the ability of MPD experiments in the visible to differentiate

Table 1: Summary of isomer differentiation criteria as a function of activation scheme and excitation conditions. The markers "−", "=" and "+", allow to describe qualitatively the contrast of a given criterion. The use of two markers is to amplify the contrast scale, e.g., for the Vis-MPD experiment performed as a function of E_{OPO} (1 pulse) at 455 nm, we showed that Y_D for Pyr^+ is much higher than for EtP^+ which is much higher than Flu^+. More simply, the boxes indicate the isomers that can be disentangled at a given criterion.

Activation	**Conditions** ***(parameter)***	**Criterion**	**Pyr^+**	**Flu^+**	**EtP^+**
CID	Helium ($t_{exc.}$)	Y_D	=	= −	=
		$R_{200/201}$	=	= +	=
	Argon ($t_{exc.}$)	Y_D	=	= +	= −
		$R_{200/201}$	=	+	= −
Vis MPD	436 nm (E_{OPO}, 1 pulse)	Y_D	=	−−	=
		$R_{200/201}$	=	= +	=
	455 nm (E_{OPO}, 1 pulse)	Y_D	++	−−	==
		$R_{200/201}$	=	= +	=
	436 nm ($t_{irr.}$, 4 mJ)	Y_D	=	−	=
		$R_{200/201}$	=	=	=
	436 nm ($t_{irr.}$, 4 mJ)	Y_D	+	−	=
		$R_{200/201}$	= −	= −	=
VUV	10.5 eV ($t_{irr.}$)	Y_D	= −	= +	=
		$R_{200/201}$	−	= −	++

isomers is superior to that of other techniques due to the possibility to excite ions at different wavelengths and thus across low and high cross sections. In addition, nonlinear effects can be used to increase the contrast between dissociation yields. VUV photoexcitation can be considered as an alternative technique but it may appear more difficult to implement. On the other hand, the commonly used CID technique does not provide much contrast in the case of the isomers studied here because the three species dissociate at comparable internal energies and only the lowest-energy dissociation channels are activated in our experimental conditions. Carrying out collisions at higher energies could be useful in this regard. An extreme case is the carbon knockout channel that opens at much higher energies ($E_{com} \sim 100$ eV in He). Stockett et al. have reported noticeable differences in this non-statistical channel for PAH isomers including $C_{16}H_{10}$, which were attributed to differences in the stability of the fragments formed by knockout.[69] However, high energy collisions are not accessible in an ion trap.

General discussion

In the discussion, we focus on fundamental aspects associated with the different excitation schemes and the impact of these schemes on the parent breakdown curves and the hydrogen loss channels for the three $C_{16}H_{10}{}^+$ isomers.

On the parent breakdown curve (I_{202} or Y_D)

The value of I_{202} is particularly useful to differentiate isomers in the MPD scheme even if the

details of this activation process remain complex. Indeed, in this scheme, several ensembles of species having absorbed a different number of photons are generated depending on the photon flux and the effective absorption cross section as shown in the case of Pyr^+ by Useli-Bacchitta et al.[58]. We have shown that the degree of non-linearity strongly depend on the combination of isomer and excitation wavelength (see Figure S10). Usually these nonlinear effects are described by fitting Y_D as a function of E_{OPO} with a power law of type $Y_D \propto E_{OPO}^n$. The value of n is considered as indicative of the number of photons needed to be absorbed to overcome the dissociation energy threshold. However, other nonlinear effects may be involved, such as a change in the absorption cross section as a function of the internal temperature of the ion,[59] which is expected to evolve throughout the interaction with the nanosecond pulse. Isomerization may also occur, especially when multiple pulses are involved.

A clear example of this complex behavior appears when comparing, in the case of Pyr^+ and EtP^+, the value of Y_D measured at $\lambda_{OPO} = 455\,nm$ in the MPD spectrum (Figure 6) to that derived in the energy dependent measurement (Figure 7(c)). In the MPD spectrum, which is obtained with five consecutive pulses at 2 mJ, Pyr^+ and EtP^+ have similar Y_D at $\lambda_{OPO} = 455\,nm$, while $Y_D(Pyr^+)$ is at least twice larger than $Y_D(EtP^+)$ for a single pulse at 10 mJ. In the first case, thermal effects due to multiple absorption across consecutive pulses may help EtP^+ to dissociate with the same efficiency than Pyr^+, possibly by favoring the formation of isomers. On the opposite, in the case of an excitation by a single pulse at 10 mJ, the multiphoton process leads Pyr^+ to dissociate more efficiently than EtP^+. This behavior, although difficult to model, provides a way to disentangle both isomers. Recently, Hrodmarsson et al.[70] used an MPD activation scheme at 620 nm to disentangle three isomers of dibenzopyrene (DBP, $C_{24}H_{14}{}^+$). The authors measured the dissociation curves as a function of the number of pulses and reported similarities but also differences in the dissociation patterns between the species studied, concluding, however, that their interpretation was not straightforward. Introducing a longer delay between pulses, as we did in our work, could have helped to disentangle the nonlinear effects from the heating between successive pulses.

We discussed above that in CID experiments, the ion absorbs energy through collisions up to an internal energy at which there is competition between the collisional and dissociation rates. The faster dissociation of Flu^+ relative to Pyr^+ observed in CID is in agreement with previous experiments using low energy[35,37] collisional activation. This behavior can be rationalized by considering the dissociation rates derived by West et al.[26]. With our model for CID, we can derive the internal energy distribution of Pyr^+ and Flu^+ while dissociating (see Figure S7). This distribution is shifted by $\sim$0.7 eV towards lower energies for Flu^+, which means that Flu^+ will start dissociating earlier than Pyr^+ upon activation by collisions. Concerning the VUV experiments, the absorption cross section of PAHs in the VUV range above 8 eV is mainly dominated by a set of $\sigma^* \leftarrow \sigma$ transitions. It is therefore smoother, and even resembles in shape and intensity that of all PAHs when renormalized by the number of carbon atoms.[71] In other words, the VUV absorption efficiency is barely useful for disentangling the isomers under study. This is well verified by the measured VUV photodissociation kinetics (Figure 9(a)) which show similar fragmentation rates between the isomers (about $2.3 \times 10^{-3}\,s^{-1}$). Yet, as in the CID experiments, Flu^+ appears to dissociate more rapidly. The VUV experiments are performed in an isolated environment in which dissociation competes with radiative cooling.[53] The difference between the kinetics curves in Figure 9(a) indicates that radiative cooling is more efficient for Pyr^+ compared to Flu^+.

For EtP^+, the stability of its neutral counterpart upon photoionization has been studied previously.[49] The authors concluded that the substituted PAH molecule has comparable stability to its non substituted counterpart. Our study provides the first insight into the dissociation properties of EtP^+. Based on the CID and VUV measurements, we can conclude

that EtP^+ has a dissociation rate close to but lower than Pyr^+, at least in the [10-12] eV energy range. However, this is only valid for the shortest activation times. For the longest activation times, our data indicate the opposite, that is, EtP^+ dissociates faster than Pyr^+. We attribute this effect to the formation of an isomer upon activation of EtP^+, which dissociates faster than the initial parent ion.

On the hydrogen fragmentation channels ($R_{200/201}$)

The $C_{16}H_9^+$ and $C_{16}H_8^+$ species are the major fragments for all three isomers and in all three activation schemes. Because $C_{16}H_8^+$ can be generated sequentially from $C_{16}H_9^+$ or directly from the parent, this channel contains information about molecular properties such as competition between the H and H_2 loss channels but it also depends on the excitation scheme which may involve fragment activation. The measured values for $R_{200/201}$ in the VUV experiments and their analysis with the kinetic model appear to be the best case for discussing differences in the dehydrogenation paths between the isomers. A high value of $R_{200/201}$ ($\sim$ 10) with almost zero evolution with irradiation time is observed for EtP^+ (Figure 9), which means that a direct channel of $2H/H_2$ loss from the parent is opened.

By fitting the dissociation curves with the kinetic model, we can construct fragmentation maps (see Figure 10) and derive a branching ratio for the $2H/H_2$ over H loss channels of the parent ions. This leads to 90%/10% and 26%/72% for EtP^+ and Flu^+. For EtP^+, these are total values that result from the contribution of the parent and its (photo)activated isomer(s). Pyr^+ has no (or a very weak) direct $2H/H_2$ loss channel, as demonstrated by some complementary measurements (see section S2.4. and Figure S13). We note that the values obtained for the branching ratio are in good agreement with the experimental $R_{200/201}$ values when extrapolated to $t_{irr.} = 0$ (approximately 9.6, 0.3, and 0 for EtP^+, Flu^+, and Pyr^+, respectively). This confirms the consistency of our kinetic model.

In CID and MPD experiments, it is more complicated to evidence and quantify a direct $2H/H_2$ loss channel. Both types of experiments provide evidence for increased values of $R_{200/201}$ in the case of Flu^+ and for specific excitation conditions. This is observed in the most highly excited conditions, which are obtained by excitation with 14 mJ laser pulses at 436 nm in MPD experiments (see Figure 7(b)) and by 3500 μs of DE in CID experiments with Ar (Figure 4 (d)). This efficient $2H/H_2$ loss of Flu^+ has indeed been observed in previous CID experiments[35,37]. It is also seen in the more recent measurements by West et al. (Figure S5 of their work and private communication).[26] The increased values of $R_{200/201}$ indicate either an efficient fragmentation of m/z=201 within the same laser pulse or that a direct channel of $2H/H_2$ loss opens at high energy for the parent at m/z=202, although we cannot conclude on this point from our data.

Rodriguez Castillo et al.[54] explored the $2H/H_2$ dehydrogenation paths in two isomers of dibenzopyrene by combining action spectroscopy under VUV photon with calculations of dissociation paths. They concluded on the presence of low-energy pathways for $2H/H_2$ loss due to the presence of bay H atoms. In this work, bay Hs refer to a configuration in which H atoms can come in close interaction although located on two different cycles. This is favored by structures called cove, bay, and fjord-regions.[72] The calculations show that the low-energy pathways for $2H/H_2$ loss involve an energy that is only 0.6-1.3 eV above the H loss channel, depending on the isomers. In the case of the non planar dibenzo(a,l)pyrene species, there is in addition a 2H loss channel at comparable energies as the H_2 channel. This is due to the stabilization of the resulting ion fragment by the formation of a five-membered ring. Although carried on different PAHs, this study brings us insights to rationalize the results of the VUV experiments. The presence of two bays in Flu^+ could account for the possibility to open the H_2 channel following absorption of VUV photons of 10.5 eV, and therefore explains the offset of 0.3 on the $R_{200/201}$ value, as dis-

cussed above. There might be also a possibility to form H_2 in the CID and MPD experiments on Flu^+, which would explain the higher values of $R_{200/201}$ that are derived for this isomer relative to the two others. Concerning EtP^+, the exceptionally high values of $R_{200/201}$ achieved in VUV experiments suggest the additional formation of a pentagonal ring at the location of the ethynyl group, although this has to be demonstrated by detailed calculations of transition states.In general, it would be interesting to explore possible dehydrogenation pathways in EtP^+ and Flu^+ using density functional theory as performed in previous studies[54,73,74]. Although out of the scope of the present article, this is a necessary step to quantify the involved energy barrier and eventually conclude on the possible role of excited states.

Conclusion

We have characterized the fragmentation features of the cations of three different $C_{16}H_{10}{}^+$ isomers using three distinct ion activation methods including activation by low energy collisions in a quadrupole ion trap, as well as visible (410 - 480 nm) multiphoton absorption and single VUV photon absorption in a cryogenic ion cyclotron resonance cell. The combination of spectral variability between the isomers and nonlinear effects makes the visible MPD technique as the best suited to disentangle the investigated PAH isomers in complex mixtures. Besides, the VUV technique consists of a more controlled experiment in which only a single photon excitation at a given energy needs to be considered. This allows to quantify the competition between the fragmentation channels for each isomer. This method is also the one that can provide data relevant for the astrophysical context. Finally, activation by low energy collisions (< 1 eV) favors the appearance of channels involving the lowest dissociation energies, i.e. the loss of a single H in our case, which is not efficient for disentangling the three isomers. Higher energy collisions can help in this regard through a better exploration of the potential energy surface of the electronic ground state.

The results presented in this paper demonstrate the value of coupling the AROMA molecular analyzer with an OPO laser to characterize the molecular structure of abundant $C_{16}H_{10}$ species observed in meteorites and laboratory analogues of interstellar/star dust. This isomer analysis may also be useful in gas-phase chemical studies to investigate the formation pathways of $C_{16}H_{10}$. To achieve this goal, we need to calibrate our instrument for samples with known isomer proportions. This is a work in progress that will be presented elsewhere. Finally, exploring the fragmentation of PAHs remains of high interest to quantify their survival in astrophysical environments. In the latter, the excitation is driven by absorption of VUV photons. Our work provides further evidence for the specificity of VUV excitation with the possible formation of a pentagonal ring in the dehydrogenation of EtP^+. This dissociation channel is not observed in the other activation schemes. It could involve highly excited states and is therefore an interesting case for dynamics studies on ultra-short time scales.

Supporting Information Available

For CID experiments: complementary CID results and figures, results of numerical simulations and modeling of breakdown curves in He, and model for the sequential H loss. For MPD experiments: complementary results for experiments as a function of pulse energy. For VUV experiments: complementary figures, full fragmentation maps for the three isomers, and experiments on the $2H/H_2$ direct loss channel for Pyr^+.

Acknowledgement The research leading to these results has received funding from the European Research Council under the European Union's Seventh Framework Programme (FP/2007-2013) ERC-2013-SyG, Grant agreement N°610256 NANOCOSMOS.

References

(1) Faccinetto, A.; Desgroux, P.; Ziskind, M.; Therssen, E.; Focsa, C. High-sensitivity detection of polycyclic aromatic hydrocarbons adsorbed onto soot particles using laser desorption/laser ionization/time-of-flight mass spectrometry: An approach to studying the soot inception process in low-pressure flames. *Combust. Flame* **2011**, *158*, 227–239.

(2) Dobbins, R. A.; Fletcher, R. A.; Benner, B. A.; Hoeft, S. Polycyclic aromatic hydrocarbons in flames, in diesel fuels, and in diesel emissions. *Combust. Flame* **2006**, *144*, 773–781.

(3) Pino, T.; Chabot, M.; Béroff, K.; Godard, M.; Fernandez-Villoria, F.; Le, K. C.; Breuer, L.; Herder, M.; Wucher, A.; Bender, M.; et al., Release of large polycyclic aromatic hydrocarbons and fullerenes by cosmic rays from interstellar dust - Swift heavy ion irradiations of interstellar carbonaceous dust analogue. *Astron. Astrophys.* **2019**, *623*, A134.

(4) Bérard, R.; Makasheva, K.; Demyk, K.; Simon, A.; Nuñez Reyes, D.; Mastrorocco, F.; Sabbah, H.; Joblin, C. Impact of metals on (star)dust chemistry: a laboratory astrophysics approach. *Front. Astron. Space Sci.* **2021**, *8*, 34.

(5) Basile, B. P.; Middleditch, B. S.; Oró, J. Polycyclic aromatic hydrocarbons in the Murchison meteorite. *Org. Geochem.* **1984**, *5*, 211–216.

(6) Naraoka, H.; Shimoyama, A.; Harada, K. Isotopic evidence from an Antarctic carbonaceous chondrite for two reaction pathways of extraterrestrial PAH formation. *Earth Planet. Sci. Lett.* **2000**, *184*, 1–7.

(7) Elsila, J. E.; de Leon, N. P.; Buseck, P. R.; Zare, R. N. Alkylation of polycyclic aromatic hydrocarbons in carbonaceous chondrites. *Geochim. Cosmochim. Acta* **2005**, *69*, 1349 – 1357.

(8) Sabbah, H.; Bonnamy, A.; Papanastasiou, D.; Cernicharo, J.; Martin-Gago, J. A.; Joblin, C. Identification of PAH isomeric structure in cosmic dust analogs: The AROMA setup. *Astrophys. J.* **2017**, *843*, 34.

(9) Shukla, B.; Koshi, M. A novel route for PAH growth in HACA based mechanisms. *Combust. Flame* **2012**, *159*, 3589–3596.

(10) Zhao, L.; Kaiser, R. I.; Xu, B.; Ablikim, U.; Ahmed, M.; Joshi, D.; Veber, G.; Fischer, F. R.; Mebel, A. M. Pyrene synthesis in circumstellar envelopes and its role in the formation of 2D nanostructures. *Nat. Astron.* **2018**,

(11) D'Anna, A. Combustion-formed nanoparticles. *Proc. Combust. Inst.* **2009**, *32*, 593–613.

(12) Sabbah, H.; Biennier, L.; Klippenstein, S. J.; Sims, I. R.; Rowe, B. R. Exploring the role of PAHs in the formation of soot: pyrene dimerization. *J. Phys. Chem. Lett.* **2010**, *1*, 2962–2967.

(13) Wang, H. Formation of nascent soot and other condensed-phase materials in flames. *Proc. Combust. Inst.* **2011**, *33*, 41–67.

(14) Desgroux, P.; Mercier, X.; Thomson, K. A. Study of the formation of soot and its precursors in flames using optical diagnostics. *Proc. Combust. Inst.* **2013**, *34*, 1713–1738.

(15) Michelsen, H. A. Probing soot formation, chemical and physical evolution, and oxidation: A review of in situ diagnostic techniques and needs. *Proc. Combust. Inst.* **2017**, *36*, 717–735.

(16) Lubman, D. M.; Kronick, M. N. Mass spectrometry of aromatic molecules with resonance-enhanced multiphoton ionization. *Anal. Chem.* **1982**, *54*, 660–665.

(17) Zhang, J.-Y.; Nagra, D. S.; Wang, A. P.; Li, L. On the capability of multiphoton ionization mass spectrometry for isomer discrimination: mass spectra of positional isomer of aromatic molecules. *Int. J. Mass Spectrom. Ion Processes* **1991**, *110*, 103–122.

(18) Zimmermann, R.; Lermer, C.; Schramm, K.; Kettrup, A.; Boesl, U. Three-dimensional trace analysis: Combination of gas chromatography, supersonic beam UV spectroscopy and time-of-flight mass spectrometry. *Eur. Mass Spectrom.* **1995**, *1*, 341–351.

(19) Carpentier, Y.; Pino, T.; Bréchignac, P. R2PI spectroscopy of aromatic molecules produced in an ethylene-rich flame. *J. Phys. Chem. A* **2013**, *117*, 10092–10104.

(20) Yang, B.; Li, Y.; Wei, L.; Huang, C.; Wang, J.; Tian, Z.; Yang, R.; Sheng, L.; Zhang, Y.; Qi, F. An experimental study of the premixed benzene/oxygen/argon flame with tunable synchrotron photoionization. *Proc. Combust. Inst.* **2007**, *31*, 555–563.

(21) Zhang, T.; Zhang, L.; Hong, X.; Zhang, K.; Qi, F.; Law, C. K.; Ye, T.; Zhao, P.; Chen, Y. An experimental and theoretical study of toluene pyrolysis with tunable synchrotron VUV photoionization and molecular-beam mass spectrometry. *Combust. Flame* **2009**, *156*, 2071–2083.

(22) Qi, F. Combustion chemistry probed by synchrotron VUV photoionization mass spectrometry. *Proc. Combust. Inst.* **2013**, *34*, 33–63.

(23) Mercier, X.; Faccinetto, A.; Batut, S.; Vanhove, G.; Božanić, D.; Hróðmarsson, H.; Garcia, G. A.; Nahon, L. Selective identification of cyclopentaring-fused PAHs and side-substituted PAHs in a low pressure premixed sooting flame by photoelectron photoion coincidence spectroscopy. *Phys. Chem. Chem. Phys.* **2020**, *22*, 15926–15944.

(24) Bourgalais, J.; Gouid, Z.; Herbinet, O.; Garcia, G. A.; Arnoux, P.; Wang, Z.; Tran, L.-S.; Vanhove, G.; Hochlaf, M.; Nahon, L.; et al., Isomer-sensitive characterization of low temperature oxidation reaction products by coupling a jet-stirred reactor to an electron/ion coincidence spectrometer: case of n-pentane. *Phys. Chem. Chem. Phys.* **2020**, *22*, 1222–1241.

(25) Bouwman, J.; Sztáray, B.; Oomens, J.; Hemberger, P.; Bodi, A. Dissociative photoionization of quinoline and isoquinoline. *J. Phys. Chem. A* **2015**, *119*, 1127–1136.

(26) West, B.; Rodriguez Castillo, S.; Sit, A.; Mohamad, S.; Lowe, B.; Joblin, C.; Bodi, A.; Mayer, P. M. Unimolecular reaction energies for polycyclic aromatic hydrocarbon ions. *Phys. Chem. Chem. Phys.* **2018**, *20*, 7195–7205.

(27) Spencer, M. K.; Hammond, M. R.; Zare, R. N. Laser mass spectrometric detection of extraterrestrial aromatic molecules: Mini-review and examination of pulsed heating effects. *Proc. Natl. Acad. Sci. U.S.A.* **2008**, *105*, 18096–18101.

(28) Sabbah, H.; Pomerantz, A. E.; Wagner, M.; Müllen, K.; Zare, R. N. Laser desorption single-photon ionization of Asphaltenes: Mass range, compound sensitivity, and matrix effects. *Energy & Fuels* **2012**, *26*, 3521–3526.

(29) Sabbah, H.; Carlos, M.; Joblin, C. Characterization of large carbonaceous molecules in cosmic dust analogues and meteorites. *Proc. Int. Astron. Union* **2019**, *15*, 103–106.

(30) Martínez, L.; Santoro, G.; Merino, P.; Accolla, M.; Lauwaet, K.; Sobrado, J.; Sabbah, H.; Pelaez, R. J.; Herrero, V. J.; Tanarro, I.; et al., Prevalence of non-aromatic carbonaceous molecules in the inner regions of circumstellar envelopes. *Nat. Astron.* **2020**, *4*, 97–105.

(31) Santoro, G.; Martínez, L.; Lauwaet, K.; Accolla, M.; Tajuelo-Castilla, G.;

Merino, P.; Sobrado, J. M.; Peláez, R. J.; Herrero, V. J.; Tanarro, I.; et al., The Chemistry of Cosmic Dust Analogs from C, C_2, and C_2H_2 in C-rich Circumstellar Envelopes. *Astrophys. J.* **2020**, *895*, 97.

(32) Jenniskens, P.; Gabadirwe, M.; Yin, Q.-Z.; Proyer, A.; Moses, O.; Kohout, T.; Franchi, F.; Gibson, R. L.; Kowalski, R.; Christensen, E. J.; et al., The impact and recovery of asteroid 2018 LA. *Meteorit. Planet. Sci.* **2021**, *56*, 844–893.

(33) Sabbah, H.; Carlos, M.; Jenniskens, P.; Shaddad, M. H.; Duprat, J.; Goodrich, C. A.; Joblin, C. Detection of Cosmic Fullerenes in the Almahata Sitta Meteorite: Are They an Interstellar Heritage? *Astrophys. J.* **2022**, *931*, 91.

(34) McLuckey, S. A.; Goeringer, D. E. Special feature: tutorial slow heating methods in tandem mass spectrometry. *J. Mass Spectrom.* **1997**, *32*, 461–474.

(35) Pyle, S. M.; Betowski, L. D.; Marcus, A. B.; Winnik, W.; Brittain, R. D. Analysis of polycyclic aromatic hydrocarbons by ion trap tandem mass spectrometry. *J. Am. Soc. Mass Spectrom.* **1997**, *8*, 183–190.

(36) Wang, X.; Becker, H.; Hopkinson, A. C.; March, R. E.; Scott, L. T.; Böhme, D. K. Collision-induced dissociation of 2-and 3-dimensional polycyclic aromatic hydrocarbon cations in a modified ion-trap detector. *Int. J. Mass Spectrom. Ion Processes* **1997**, *161*, 69–76.

(37) Mansoori, B. A. Isomeric identification and quantification of polycyclic aromatic hydrocarbons in environmental samples by liquid chromatography tandem mass spectrometry using a high pressure quadrupole collision cell. *Rapid Commun. Mass Spectrom.* **1998**, *12*, 712–728.

(38) Oomens, J.; Tielens, A. G. G. M.; Sartakov, B. G.; von Helden, G.; Meijer, G. Laboratory infrared spectroscopy of cationic polycyclic aromatic hydrocarbon molecules. *Astrophys. J.* **2003**, *591*, 968–985.

(39) Oomens, J.; Sartakov, B. G.; Meijer, G.; von Helden, G. Gas-phase infrared multiple photon dissociation spectroscopy of mass-selected molecular ions. *Int. J. Mass Spectrom.* **2006**, *254*, 1–19.

(40) Alvaro Galué, H.; Oomens, J. On the electronic structure of isolated monodehydrogenated polyaromatic hydrocarbon ions and their astrophysical relevance. *Astrophys. J.* **2012**, *746*, 83.

(41) de Haas, A. J.; Oomens, J.; Bouwman, J. Facile pentagon formation in the dissociation of polyaromatics. *Phys. Chem. Chem. Phys.* **2017**, *19*, 2974–2980.

(42) Jusko, P.; Simon, A.; Banhatti, S.; Brünken, S.; Joblin, C. Direct evidence of the benzylium and tropylium cations as the two long-lived isomers of $C_7H_7^+$. *ChemPhysChem* **2018**, *19*, 3182–3185.

(43) Jusko, P.; Simon, A.; Wenzel, G.; Brünken, S.; Schlemmer, S.; Joblin, C. Identification of the fragment of the 1-methylpyrene cation by mid-IR spectroscopy. *Chem. Phys. Lett.* **2018**, *698*, 206–210.

(44) Wenzel, G.; Simon, A.; Banhatti, S.; Jusko, P.; Schlemmer, S.; Brünken, S.; Joblin, C. Infrared spectroscopy of the benzylium-like (and tropylium-like) isomers formed in the –H dissociative ionization of methylated PAHs. *J. Mol. Spectrosc.* **2022**, *385*, 111620.

(45) Jochims, H. W.; Ruhl, E.; Baumgartel, H.; Tobita, S.; Leach, S. Size effects on dissociation rates of polycyclic aromatic hydrocarbon cations: Laboratory studies and astrophysical implications. *Astrophys. J.* **1994**, *420*, 307.

(46) Jochims, H. W.; Baumgärtel, H.; Leach, S. Structure-dependent photostability of polycyclic aromatic hydrocarbon cations:

Laboratory Studies and astrophysical Implications. *Astrophys. J.* **1999**, *512*, 500–510.

(47) West, B.; Joblin, C.; Blanchet, V.; Bodi, A.; Sztáray, B.; Mayer, P. M. On the dissociation of the naphthalene radical cation: new iPEPICO and tandem mass spectrometry results. *J. Phys. Chem. A* **2012**, *116*, 10999–11007.

(48) West, B.; Sit, A.; Mohamed, S.; Joblin, C.; Blanchet, V.; Bodi, A.; Mayer, P. M. Dissociation of the anthracene radical cation: a comparative look at iPEPICO and collision-induced dissociation mass spectrometry results. *J. Phys. Chem. A* **2014**, *118*, 9870–9878.

(49) Rouillé, G.; Krasnokutski, S. A.; Fulvio, D.; Jäger, C.; Henning, T.; Garcia, G. A.; Tang, X.-F.; Nahon, L. Dissociative photoionization of polycyclic aromatic hydrocarbon molecules carrying an ethynyl group. *Astrophys. J.* **2015**, *810*, 114.

(50) Rouillé, G.; Steglich, M.; Hemberger, P.; Jäger, C.; Henning, T. Threshold dissociation of the 1-ethynylpyrene cation at internal energies relevant to H I regions. *Astrophys. J.* **2019**, *885*, 21.

(51) Zhen, J.; Rodriguez Castillo, S.; Joblin, C.; Mulas, G.; Sabbah, H.; Giuliani, A.; Nahon, L.; Martin, S.; Champeaux, J.-P.; Mayer, P. M. VUV Photo-processing of PAH cations: Quantitative study on the ionization versus fragmentation processes. *Astrophys. J.* **2016**, *822*, 113.

(52) Wenzel, G.; Joblin, C.; Giuliani, A.; Rodriguez Castillo, S.; Mulas, G.; Ji, M.; Sabbah, H.; Quiroga, S.; Peña, D.; Nahon, L. Astrochemical relevance of VUV ionization of large PAH cations. *Astron. Astrophys.* **2020**, *641*, A98.

(53) Marciniak, A.; Joblin, C.; Mulas, G.; Mundlapati, V. R.; Bonnamy, A. Photodissociation of aliphatic PAH derivatives under relevant astrophysical conditions. *Astron. Astrophys.* **2021**, *652*, A42.

(54) Rodriguez Castillo, S.; Simon, A.; Joblin, C. Investigating the importance of edge-structure in the loss of H/H_2 of PAH cations: The case of dibenzopyrene isomers. *Int. J. Mass Spectrom.* **2018**, *429*, 189–197.

(55) Joblin, C.; Pech, C.; Armengaud, M.; Frabel, P.; Boissel, P. A piece of interstellar medium in the laboratory: the PIRENEA experiment. EAS Pub. Ser. 2002; pp 73–77.

(56) West, B.; Useli-Bacchitta, F.; Sabbah, H.; Blanchet, V.; Bodi, A.; Mayer, P. M.; Joblin, C. Photodissociation of pyrene cations: Structure and energetics from $C_{16}H_{10}^+$ to C_{14}^+ and almost everything in between. *J. Phys. Chem. A* **2014**, *118*, 7824–7831.

(57) Marshall, A. G.; Hendrickson, C. L.; Jackson, G. S. Fourier transform ion cyclotron resonance mass spectrometry: A primer. *Mass Spectrom. Rev.* **1998**, *17*, 1–35.

(58) Useli-Bacchitta, F.; Bonnamy, A.; Mulas, G.; Malloci, G.; Toublanc, D.; Joblin, C. Visible photodissociation spectroscopy of PAH cations and derivatives in the PIRENEA experiment. *Chem. Phys.* **2010**, *371*, 16–23.

(59) Stockett, M. H.; Björkhage, M.; Cederquist, H.; Schmidt, H. T.; Zettergren, H. Storage time dependent photodissociation action spectroscopy of polycyclic aromatic hydrocarbon cations in the cryogenic electrostatic storage ring DESIREE. *Faraday Discuss.* **2019**, *217*, 126–137.

(60) Drahos, L.; Vékey, K. MassKinetics: a theoretical model of mass spectra incorporating physical processes, reaction kinetics and mathematical descriptions. *J. Mass Spectrom.* **2001**, *36*, 237–263.

(61) Muntean, F.; Armentrout, P. Guided ion beam study of collision-induced dissociation dynamics: integral and differential cross sections. *J. Chem. Phys.* **2001**, *115*, 1213–1228.

(62) Pollreisz, F.; Ágnes Gömöry,; Sztáray, J.; Végh, P.; Drahos, L.; Kiss, A.; Vékey, K. Very high critical energy fragmentations observed in CID. *Int. J. Mass Spectrom.* **2005**, *243*, 41–47.

(63) Laskin, J.; Byrd, M.; Futrell, J. Internal energy distributions resulting from sustained off-resonance excitation in FTMS. I. Fragmentation of the bromobenzene radical cation. *Int. J. Mass Spectrom.* **2000**, *195*, 285–302.

(64) Heeren, R. M. A.; Vékey, K. A novel method to determine collisional energy transfer efficiency by Fourier transform ion cyclotron resonance mass spectrometry. *Rapid Commun. Mass Spectrom.* **1998**, *12*, 1175–1181.

(65) Basic, C.; Yost, R. A. Collision-induced dissociation breakdown surfaces for n-alkylbenzene molecular ions in a quadrupole ion trap mass spectrometer. *Int. J. Mass Spectrom.* **2000**, *194*, 121–132.

(66) Biennier, L.; Salama, F.; Gupta, M.; O'Keefe, A. Multiplex integrated cavity output spectroscopy of cold PAH cations. *Chem. Phys. Lett.* **2004**, *387*, 287–294.

(67) Salama, F.; Allamandola, L. Is a pyrene-like molecular ion the cause of the 4,430-Å diffuse interstellar absorption band? *Nature* **1992**, *358*, 42–43.

(68) Naganathappa, M.; Chaudhari, A. Theoretical infrared and electronic absorption spectra of $C_{16}H_{10}$ isomers, their ions and doubly ions. *Mon. Not. Roy. Astron. Soc.* **2012**, *425*, 490–505.

(69) Stockett, M. H.; Gatchell, M.; de Ruette, N.; Giacomozzi, L.; Chen, T.; Rousseau, P.; Maclot, S.; Chesnel, J.-Y.; Adoui, L.; Huber, B., et al. Isomer effects in fragmentation of polycyclic aromatic hydrocarbons. *Int. J. Mass Spectrom.* **2015**, *392*, 58–62.

(70) Hrodmarsson, H. R.; Bouwman, J.; Tielens, A. G. M.; Linnartz, H. Similarities and dissimilarities in the fragmentation of polycyclic aromatic hydrocarbon cations: A case study involving three dibenzopyrene isomers. *Int. J. Mass Spectrom.* **2022**, 116834.

(71) Malloci, G.,; Mulas, G.,; Joblin, C., Electronic absorption spectra of PAHs up to vacuum UV - Towards a detailed model of interstellar PAH photophysics. *Astron. Astrophys.* **2004**, *426*, 105–117.

(72) Ehrenhauser, F. S. PAH and IUPAC Nomenclature. *Polycycl Aromat Compd* **2015**, *35*, 161–176.

(73) Jolibois, F.; Klotz, A.; Gadéa, F. X.; Joblin, C. Hydrogen dissociation of naphthalene cations: a theoretical study. *A&A* **2005**, *444*, 629–634.

(74) Castellanos, P.; Candian, A.; Zhen, J.; Linnartz, H.; Tielens, A. G. G. M. Photoinduced polycyclic aromatic hydrocarbon dehydrogenation The competition between H- and H_2-loss. *Astron. Astrophys.* **2018**, *616*, A166.

TOC Graphic

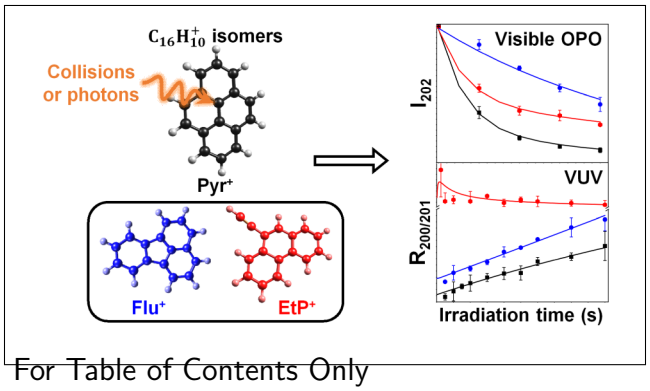

For Table of Contents Only

Supporting Information:

Isomer Differentiation of Trapped $C_{16}H_{10}^+$ Using Low-Energy Collisions and Visible/VUV Photons

M. Viswanathan Vinitha,[†,¶] Venkateswara Rao Mundlapati,[†,¶] Alexandre Marciniak,[†,‡,¶] Mickaël Carlos,[†] Hassan Sabbah,[†] Anthony Bonnamy,[†] Loïc Noguès,[†] David Murat,[†] Odile Coeur-Joly,[†] and Christine Joblin[*,†]

†*Institut de Recherche en Astrophysique et Planétologie (IRAP), Université Toulouse III - Paul Sabatier, CNRS, CNES, 9 Avenue du Colonel Roche, F-31028 Toulouse, France*

‡*Current address: Laboratoire Collisions Agrégats Réactivité (LCAR/IRSAMC), Université Toulouse III - Paul Sabatier, CNRS, 118 Route de Narbonne, F-31062 Toulouse, France*

¶*These authors have equally contributed*

E-mail: christine.joblin@irap.omp.eu

S1. Complementary CID results

S1.1. CID Experiments

Examples of mass spectra obtained for CID experiments of Pyr^+ in He and Ar are shown in Figure S1. The kinetic or breakdown curves of $C_{16}H_{10}^+$ isomers obtained for CID in He and Ar are presented in Figure S2 and Figure S3, respectively.

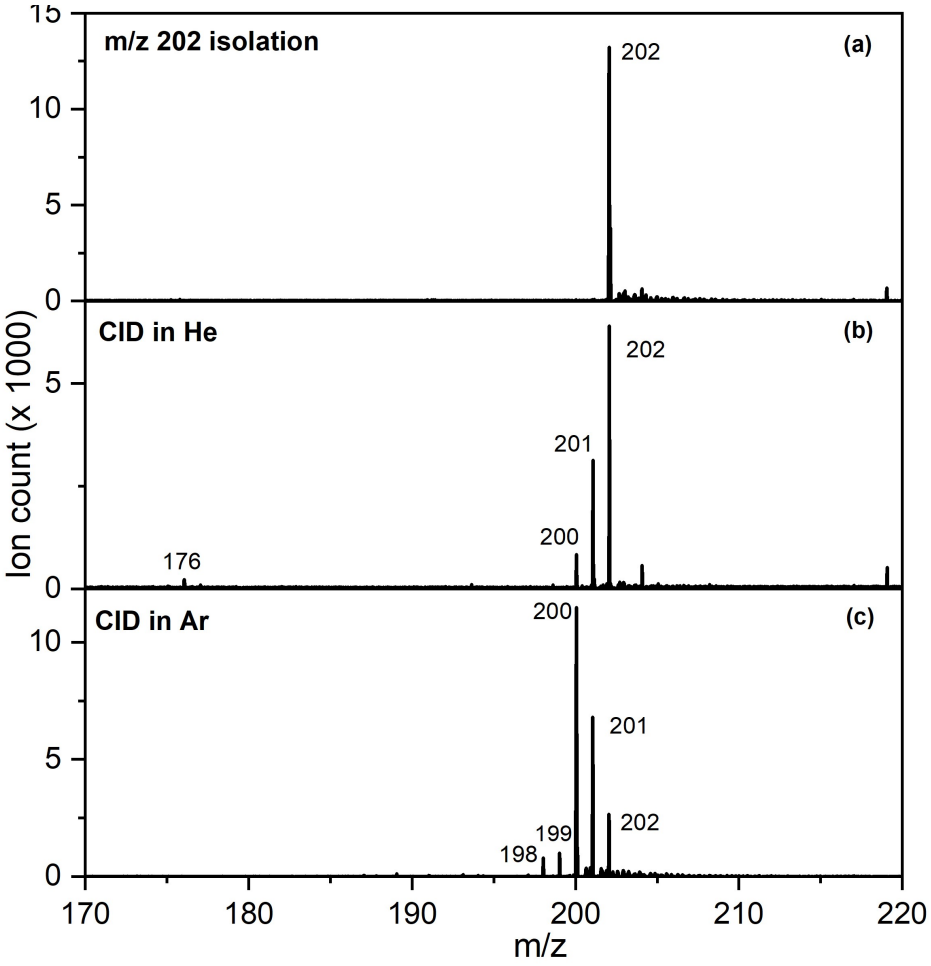

Figure S1: (a) Mass spectrum where the pure ^{12}C isotopomer of Pyr^+ was isolated. (b) Example of mass spectrum measured for the same species after CID in He and an excitation time of 4.75 ms (the recorded m/z range was [170-220] in this measurement). (c) Example of a mass spectrum measured after CID in Ar for an excitation time of 3.5 ms. The m/z detection range was [190-210] in this last measurement which explains why no carbon loss fragments can be observed here.

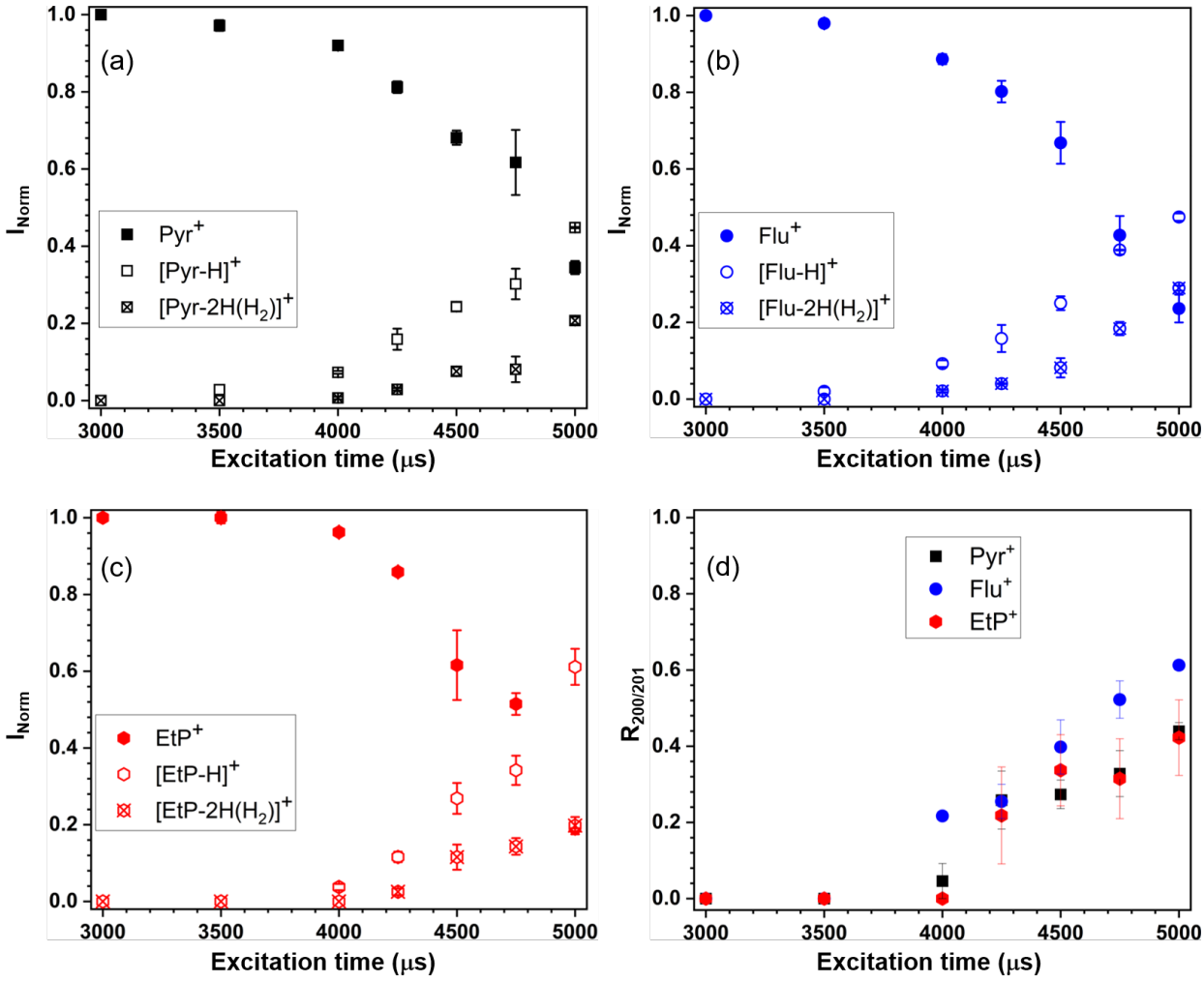

Figure S2: Normalized ion intensities of (a) Pyr^+, (b) Flu^+, and (c) EtP^+ and their first fragments (H and $2H/H_2$ loss channels) for CID in He as a function of the dipolar excitation time. (d) Evolution of the intensity ratio corresponding to the $2H/H_2$ over H loss channels ($R_{200/201}$).

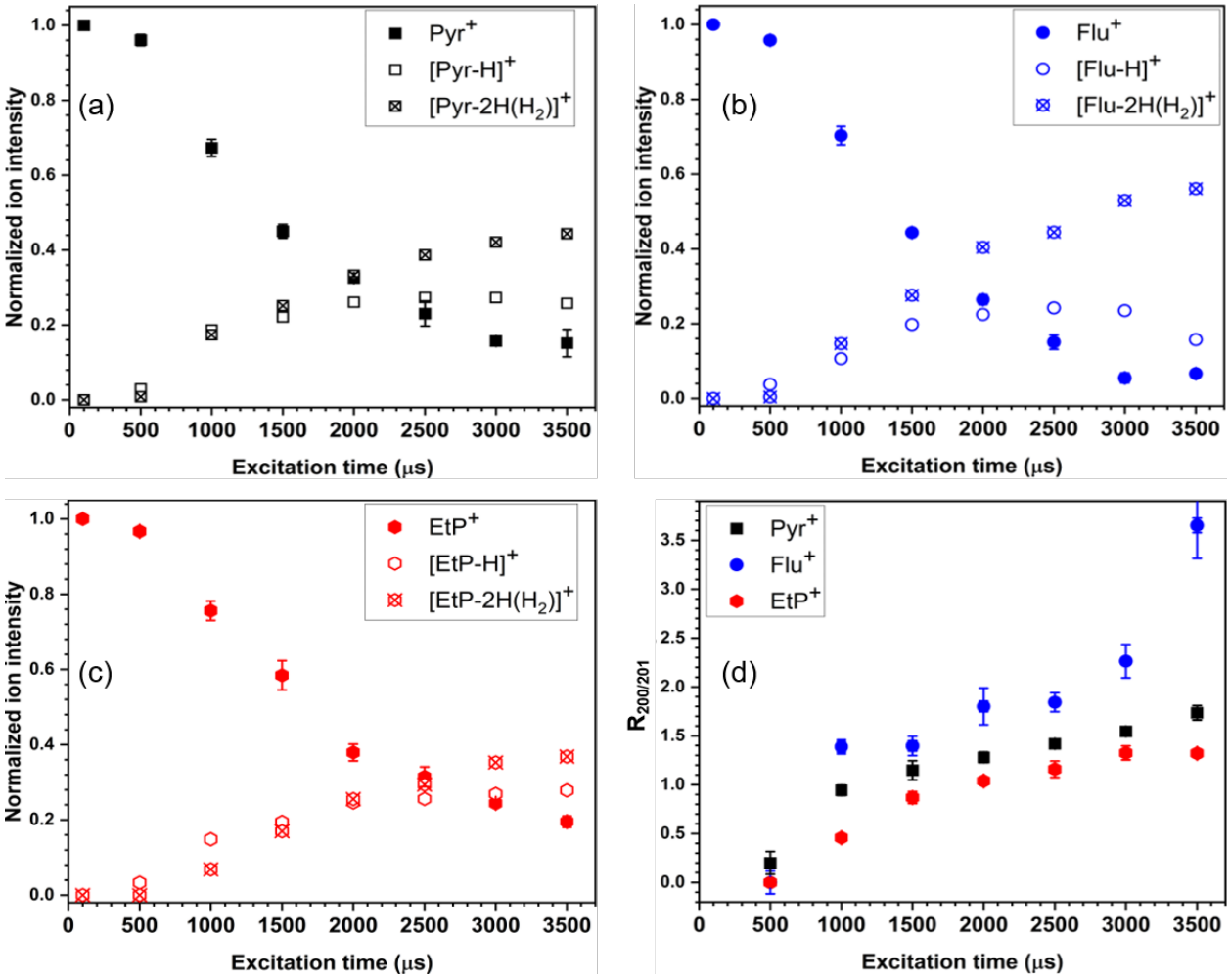

Figure S3: Normalized ion intensities of (a) Pyr^+, (b) Flu^+, and (c) EtP^+ and their first fragments (H and $2H/H_2$ loss channels) for CID in Ar as a function of the dipolar excitation time. (d) Evolution of the intensity ratio corresponding to the $2H/H_2$ over H loss channels ($R_{200/201}$).

S1.2. Modeling CID breakdown curves

To mimic the experimental conditions, the model for CID was run at a rare gas pressure of 10^{-3} mbar and a DE frequency of 206.5 and 205.5 kHz, for He and Ar, respectively. The value of 206.5 kHz corresponds to the frequency at which the ions gain the maximum kinetic energy in the simulations. It differs by about 10% from the resonance frequency used in the experiments, due to an imperfect description of the ion trap in Simion©. The distributions of collision energies in the center-of-mass frame, E_{com}, and time interval between collisions, t_{coll}, which were recovered from Simion© simulations, are displayed in Figure S4.

Figure S5 (a) shows, in the case of CID in He, the breakdown curves of the three isomers that were fitted by performing Monte Carlo simulations (see description in the main manuscript). The time variation of the internal energy distribution of Pyr^+ ions obtained from this simulation is presented in Figure S5 (b). The values for the free parameter η derived from the simulations to fit the experimental data (Figure 5(a) of the main manuscript and Figure S5 (a)) are shown in Figure S6 for both He and Ar. Finally, Figure S7 compares, in the case of Pyr^+ and Flu^+, the internal energy distribution for dissociating ions (when $k_{coll} < k_{diss}(U)$) derived from the Monte Carlo simulations.

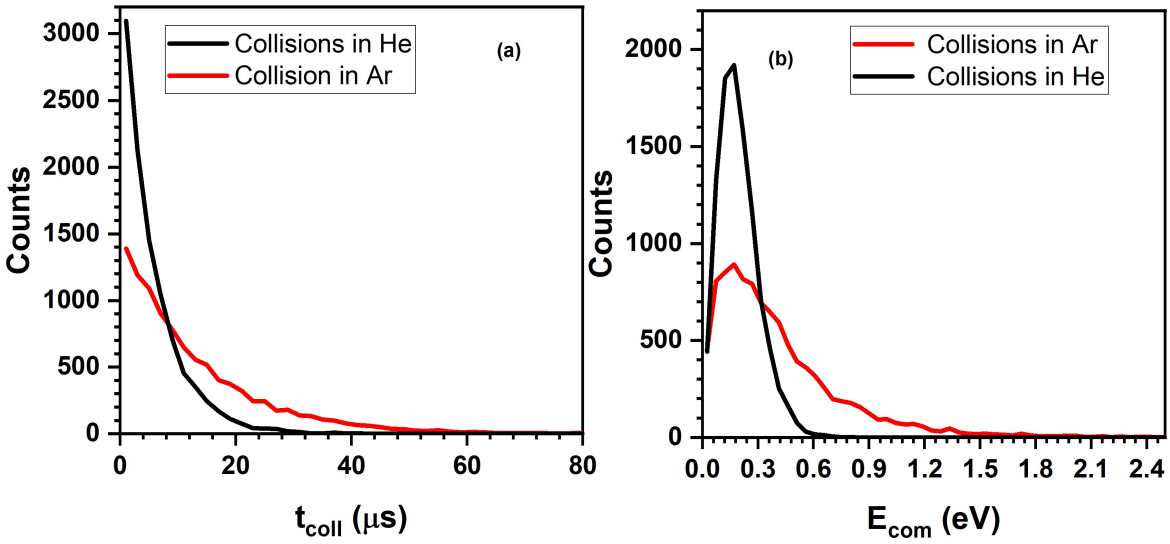

Figure S4: (a) Distribution of time interval between two collisions (t_{coll}) for CID in He and Ar simulated by Simion©. (b) Distribution of collision energy (E_{com}) for CID in He and Ar simulated by Simion©.

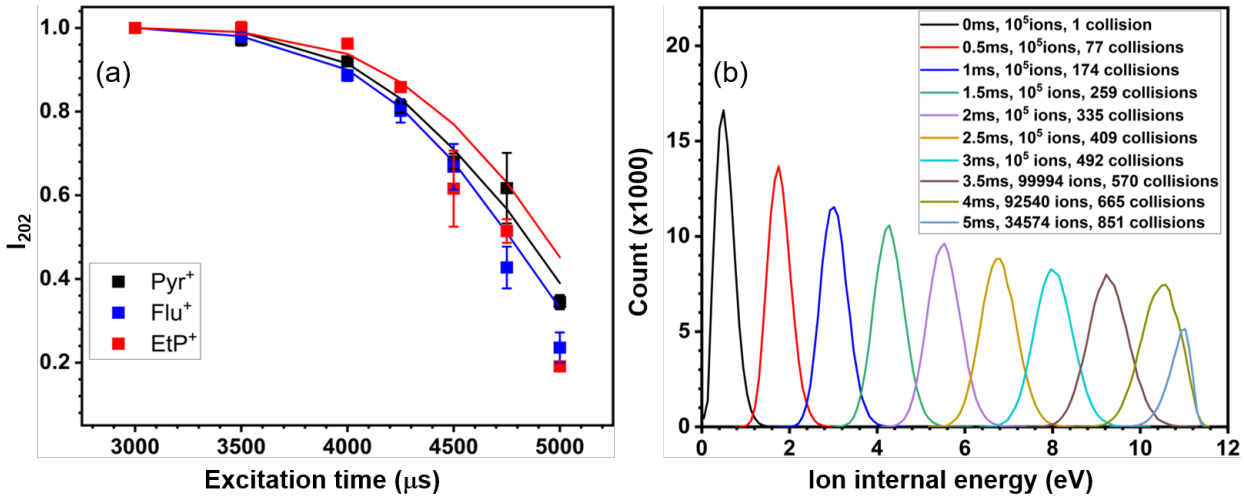

Figure S5: Model simulation results for CID in He. (a) Fitted breakdown curves (solid line) for the three isomeric ions. Experimental data points are shown as scattered dots. (b) Internal energy distribution of Pyr^+ as a function of the excitation time.

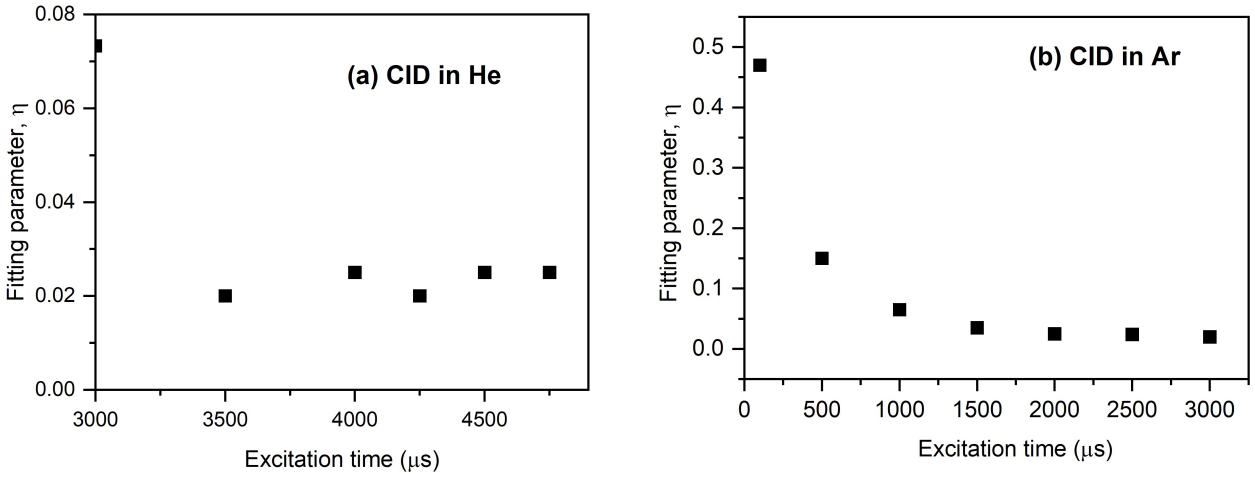

Figure S6: Time variation of the η parameter, derived from fitting experimental data with Monte Carlo simulations for CID in (a) He and (b) Ar.

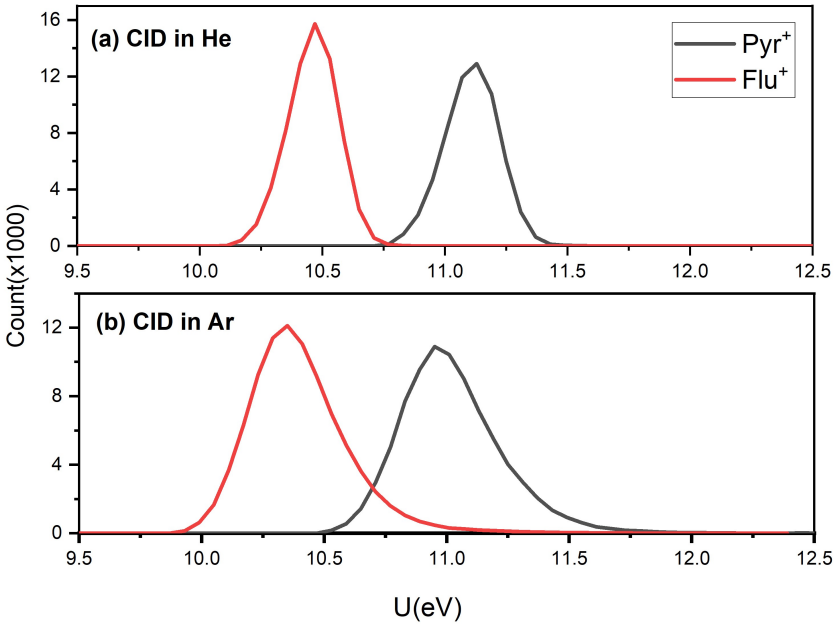

Figure S7: Simulated internal energy distribution of dissociating ions in the case of Pyr^+ and Flu^+ and for the CID experiment in (a) He and (b) Ar.

S1.3. Modeling sequential H loss curves for CID in He

We modeled the measured H and 2H loss curves for CID in He using a simple semi-empirical method. The method assumes that the parent ions mainly depopulate by single hydrogen loss so that the instantaneous production of -H fragment ions can be easily derived from the parent breakdown curves. The 2H loss ion yield curve is then computed by doing a convolution between the yield of -H fragment and its breakdown curve. The latter is obtained from the previous simulations by using the η parameter derived for the parent ions and the dissociation rates of the -H fragment available in West et al.[S1]. Since the H loss rate of $[EtP\text{-}H]^+$ is not available from the latter study, the breakdown curve of $[EtP\text{-}H]^+$ was built using the H loss rate of $[Pyr\text{-}H]^+$. This choice is justified by the fact that the values of $R_{200/201}$ for these two isomers are found to be similar for CID in He (see Figure 4(b)).

We initially modeled the 2H loss curves by assuming that the ions are produced at room temperature after H loss and undergo subsequent collisional heating. This resulted in a calculated 2H loss curve that is delayed in time from the experimental curve, showing that the -H ions are produced with a significant amount of internal energy. To simply account for this effect, we shifted the modeled curves in time to match the timing of the experimental curves. As shown in Figure S8, the two types of curves are then consistent, supporting a scenario of sequential H loss under slow CID heating. In the case of CID in Ar, the high values reached for $R_{200/201}$ and the very slow increase of this ratio with excitation time (Figure 4 (d)) can be attributed to fast excitation of -H fragments.

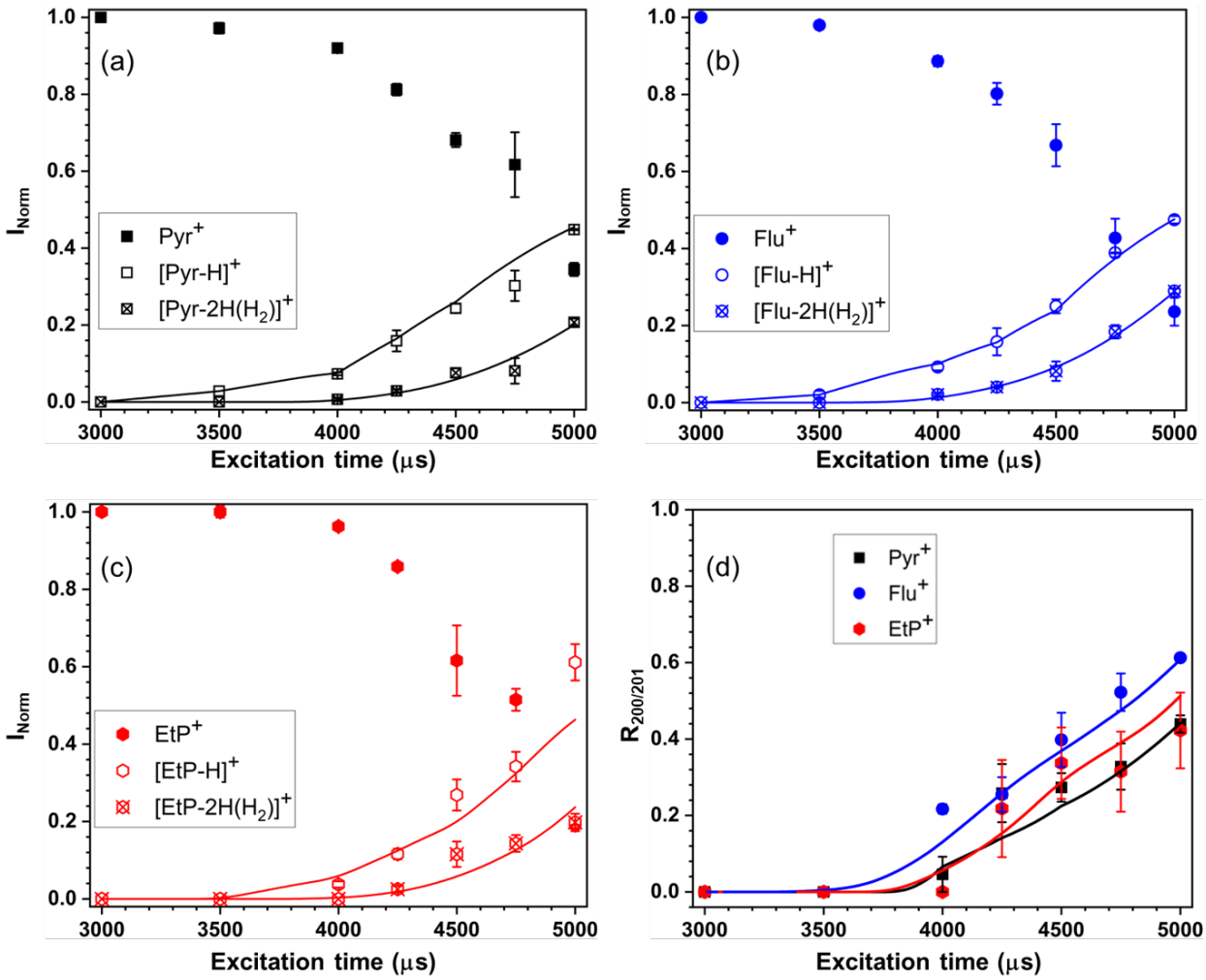

Figure S8: CID experiments in He gas: parent breakdown curve and relative abundance of H and 2H loss channels as a function of excitation time for (a) Pyr^+, (b) Flu^+, and (c) EtP^+. (d) Ratio of associated fragments $R_{200/201}$. The solid lines were obtained with a semi-empirical model that describes the sequential loss of H (see S1.3.)

S2. Complementary photoexcitation results

S2.1. Visible MPD results: Pulse energy dependent breakdown curves

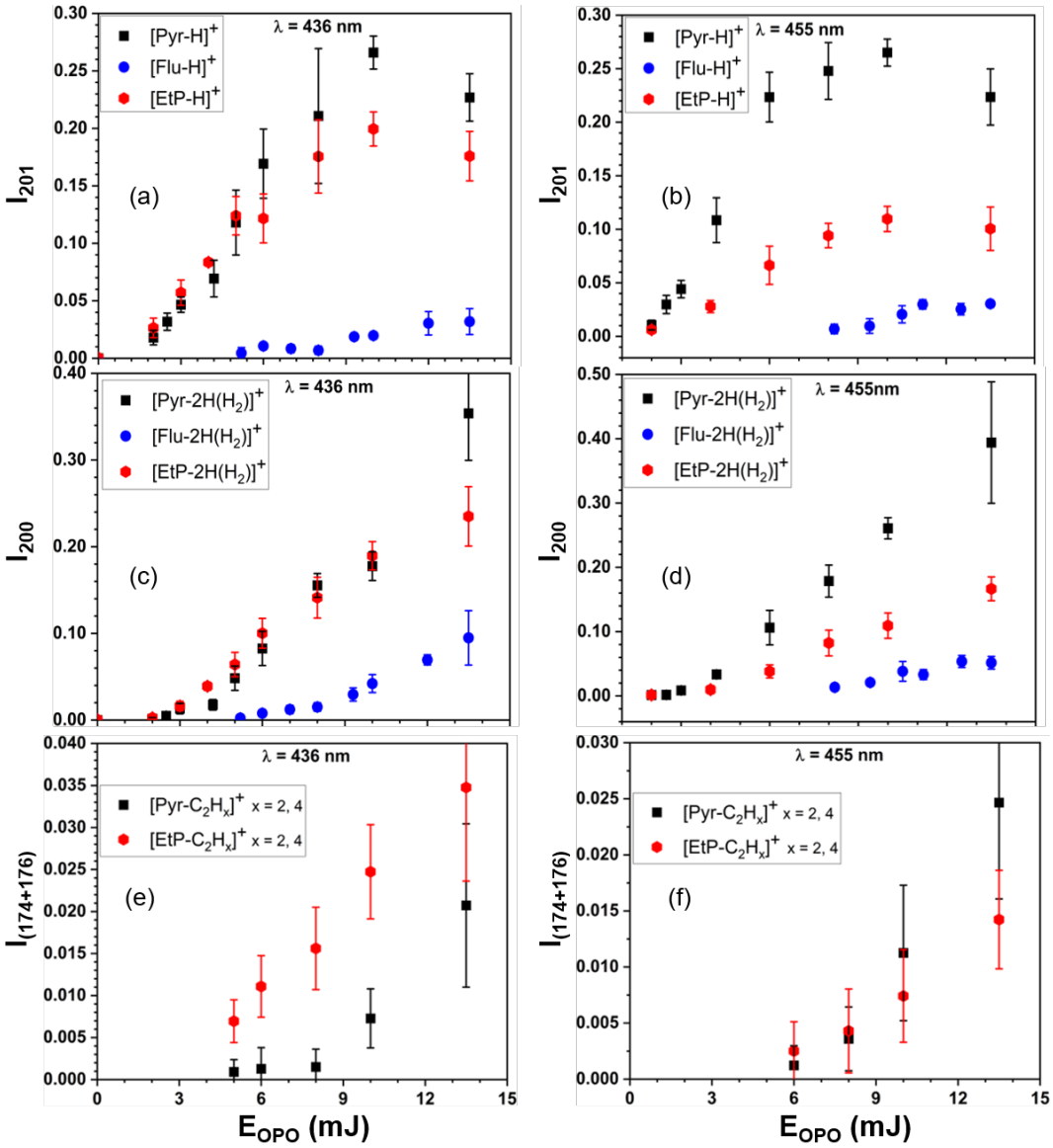

Figure S9: Normalized ion intensities of (a-b) H, (c-d) $2H/H_2$ and (e-f) C_2H_2 loss channels for the three isomers at 436 nm (left column) and 455 nm (right column). In the case of Flu^+, the C_2H_2 loss channel was not detected even at the highest pulse energy. Dehydrogenated fragments ($C_{16}H^+_{10-x}$) are observed up to $x = 4$ for Pyr^+ and EtP^+, in agreement with West et al.[S2], while only up to $x = 2$ is observed for Flu^+.

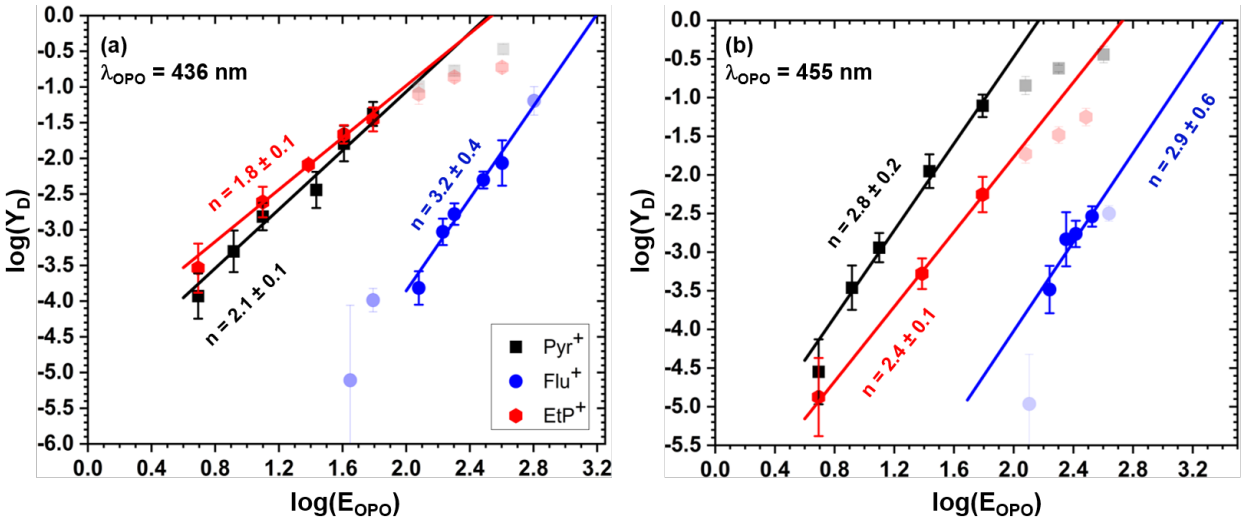

Figure S10: Dissociation efficiency Y_D of the three isomers as a function of pulse energy from data recorded at (a) 436 nm and (b) 455 nm (Figure 7 of the main manuscript). The use of a log-log scale allows us to define a linear regime with a slope n that quantifies the increase of Y_D with laser energy, considering that $Y_D \propto (E_{OPO})^n$. The transparent points are those that have not been taken into account in the fit. We obtained $n = 2.8 \pm 0.1$ for Pyr^+ at 455 nm, which agrees well with the value obtained by Wolf et al.[S3] in similar experiments.

S2.2. VUV breakdown curve of the parent, and H and 2H/H_2 loss channels

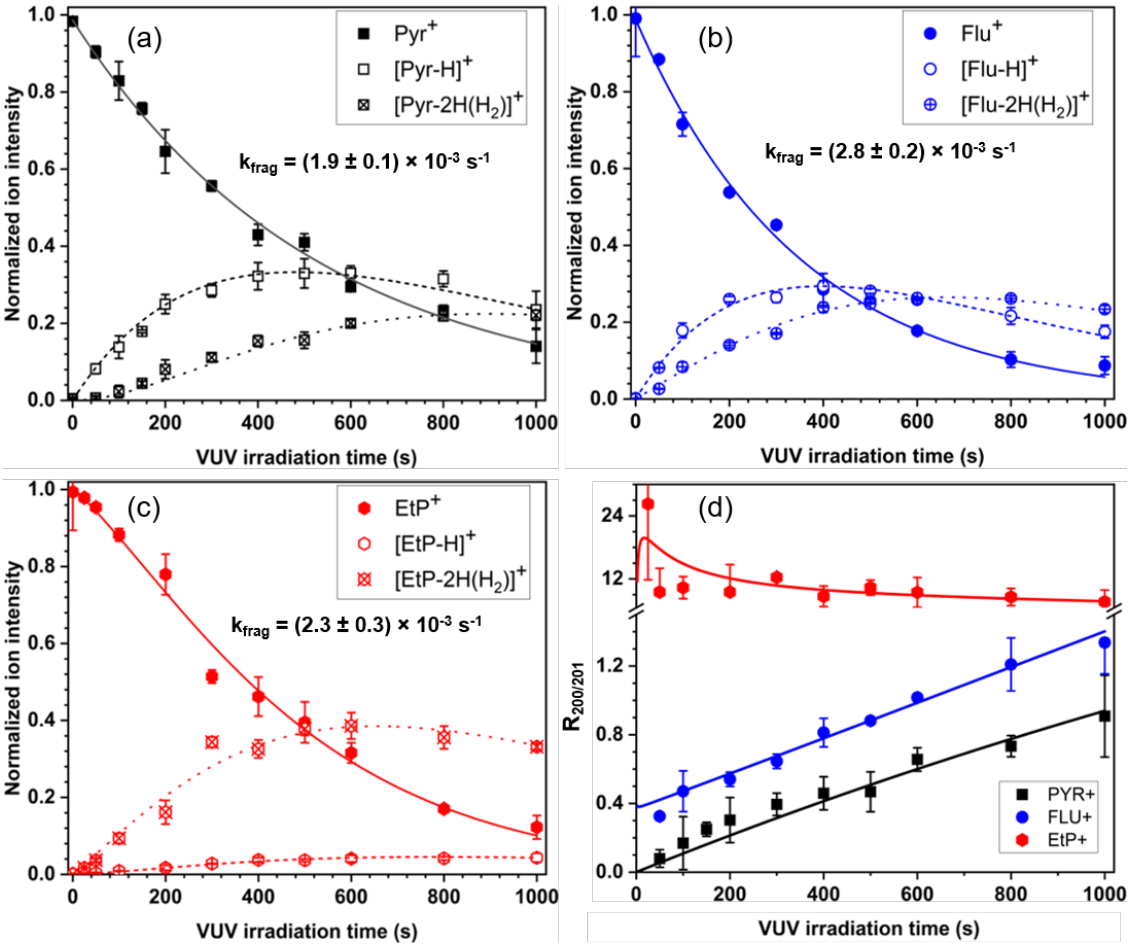

Figure S11: Normalized ion intensities of (a) Pyr^+, (b) Flu^+, and (c) EtP^+ and their first fragmentation channels (H and 2H/H_2 loss) as a function of VUV irradiation time. The fit curves and the extracted fragmentation rates for each parent isomer are displayed. (d) Evolution of the intensity ratio corresponding to the 2H/H_2 over H loss channels ($R_{200/201}$) as a function of the VUV irradiation time.

S2.3. Full Fragmentation map of three isomers

In Figure S12(a-c), we display the full fragmentation maps of each isomer obtained thanks to the fitting procedure using the kinetic model (see main paper). They correspond to the complete versions of the simplified fragmentation maps displayed in Figure 10 of the main paper. For Pyr^+ and Flu^+, we are confident in the obtained maps and their extracted fragmentation rates since the experimental data constrain them well. We believe that only minor additional channels may exist, but they will not be sufficiently constrained by our experimental data to extract relevant parameters (e.g., the direct $2H/H_2$ loss pathway in Pyr^+).

For EtP^+, the parent breakdown curve shows a "delay" before having a standard exponential decay behavior. We model this by a population of photoactivated isomers (EtP^{+*}) that is built when the inactivated EtP^+ ions absorb a first VUV photon. The various tests of the model performed before obtaining the displayed map revealed that this isomer channel competes with a direct $2H/H_2$ loss channel. However, in order to construct this map (Figure S12(c)), we had to set an upper limit for the fragmentation rates to stay within limits consistent with the VUV flux and an estimate of the EtP^+ photo-absorption cross section at 10.5 eV. By relaxing this constraint, we obtain the fragmentation map shown in Figure S12(d) and we also gain in quality of fit (from $R^2 = 0.9869$ to $R^2 = 0.9892$). We observe that the branching ratio between the direct $2H/H_2$ loss channel and the isomerization channel changes from 28 %/72 % to 12 %/88 % and that the initial populations of EtP^+ and EtP^{+*} also change from 93 %/7 % to 100 %/0 %. This shows that some of the fitting parameters are interdependent and that the obtained rates should be taken with caution. More importantly, the fragmentation rate of the EtP^{+*} population reaches a value of $14 \times 10^{-3}\,s^{-1}$, in particular due to the strong contribution of the $2H/H_2$ loss channel (about $11.2 \times 10^{-3}\,s^{-1}$). This extracted fragmentation rate is exceptionally high compared to standard values (about $3 \times 10^{-3}\,s^{-1}$) for PAHs that efficiently absorb VUV photons and consecutively fragment without competition from radiative cooling (e.g. see Marciniak et al.[S4]). We do not have a clear interpretation for this result. It could suggest that the isomer produced (EtP^{+*}) is metastable on a second timescale. Such an assumption is still consistent with the claim that there is competition between a direct

$2H/H_2$ loss and isomerization. Note that the other fragmentation rates hardly change between the two EtP^+ maps (Figure S12(c-d)). Finally, as it was done for the coronene cation in Marciniak et al.[S4], we tried a model in which we added a channel back from the isomer population to the initial population. This model also works well. Nevertheless, the addition of a rate makes the free parameters even more interdependent and does not allow us to conclude on the existence of this additional channel. Obtaining evidence for this specific channel remains a limitation of the kinetic model we use in this study.

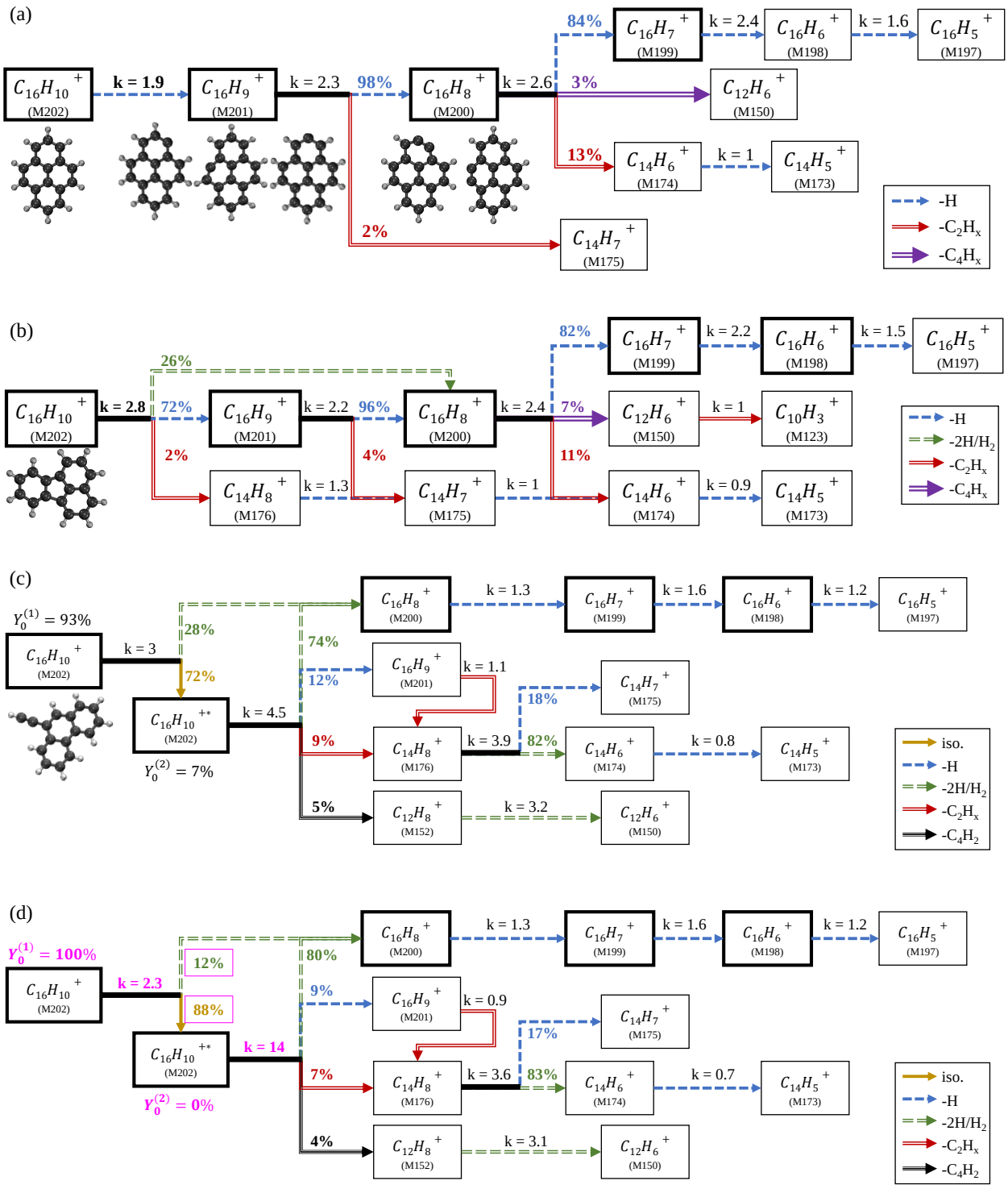

Figure S12: Complete fragmentation map of (a) Pyr^+, (b) Flu^+, and (c) EtP^+. Each arrow represents a fragment loss or a mechanism triggered by the absorption of a VUV photon (see legend in each map). We display the fragmentation rate of each ion channel (written k to simplify and rounded to the first decimal) in $\times 10^{-3}$ s^{-1} and the branching ratios (rounded to their integer values). The bold boxes correspond to the main ion channels (yield greater than 10 % during kinetics). The case of EtP^+ is special since the fit requires the contribution of a population of photoactivated isomers that delay the fragmentation kinetics. Another likely version of this map is shown in (d). The main differences between these two maps are highlighted in magenta.

S2.4. Search for a direct $2H/H_2$ loss channel in Pyr^+

To clarify the presence of a direct $2H/H_2$ loss channel in the Pyr^+ fragmentation map ($Pyr^+ \rightarrow [Pyr\text{-}2H/H_2]^+$), we performed specific measurements in which we repeatedly ejected the $[Pyr\text{-}H]^+$ fragments irradiation of the trapped ion cloud. Note that the ejection procedure can disturb the ion cloud, so we did not apply a continuous ejection of $[Pyr\text{-}H]^+$ fragments. As a compromise, we chose to eject the $[Pyr\text{-}H]^+$ fragments every 25 s during the VUV irradiation. As it is shown in Figure S13 (a), this delay is short enough to avoid the production of $[Pyr\text{-}2H/H_2]^+$ by sequential dissociation ($Pyr^+ \rightarrow [Pyr\text{-}H]^+ \rightarrow [Pyr\text{-}2H/H_2]^+$). In Figure S13 (b-d), we compare the mass spectra obtained for a VUV irradiation time of 200, 400, and 600 s respectively when no ejection is performed (”reference”, black curve) with those obtained when an ejection is performed every 25 s (”direct”, red curve). Each mass spectrum has been normalized to the Pyr^+ intensity in order to compare the ”reference” and ”direct” measurements at a given VUV irradiation time. The figures show that a direct $2H/H_2$ loss channel, if it exists, is very small: a zoom on the scale 0 - 2 % must be performed to observe the $[Pyr\text{-}2H/H_2]^+$ signal. To quantify the branching ratio between this channel and the H loss (and the sequential cascade), we defined the following ratio:

$$R_{-2H/H_2,direct} = \frac{I_{-2H/H_2,direct}}{I_{-H,ref} + I_{-2H/H_2,ref}} \quad (1)$$

where $I_{-H,ref} + I_{-2H/H_2,ref}$ is the sum of the intensity of the -H and $-2H/H_2$ channels in the reference measurement (black curve) and $I_{-2H/H_2,direct}$ is the intensity of the $2H/H_2$ loss channel when ejection of the $[Pyr\text{-}H]^+$ is performed. This ratio is shown in Figure S13 (e) for the three VUV irradiation times. The average is $R_{2H/H_2,direct} = 1.9 \pm 1.4\%$. As it is small, we decided not to consider this channel in the fragmentation map in agreement with Marciniak et al.[S4].

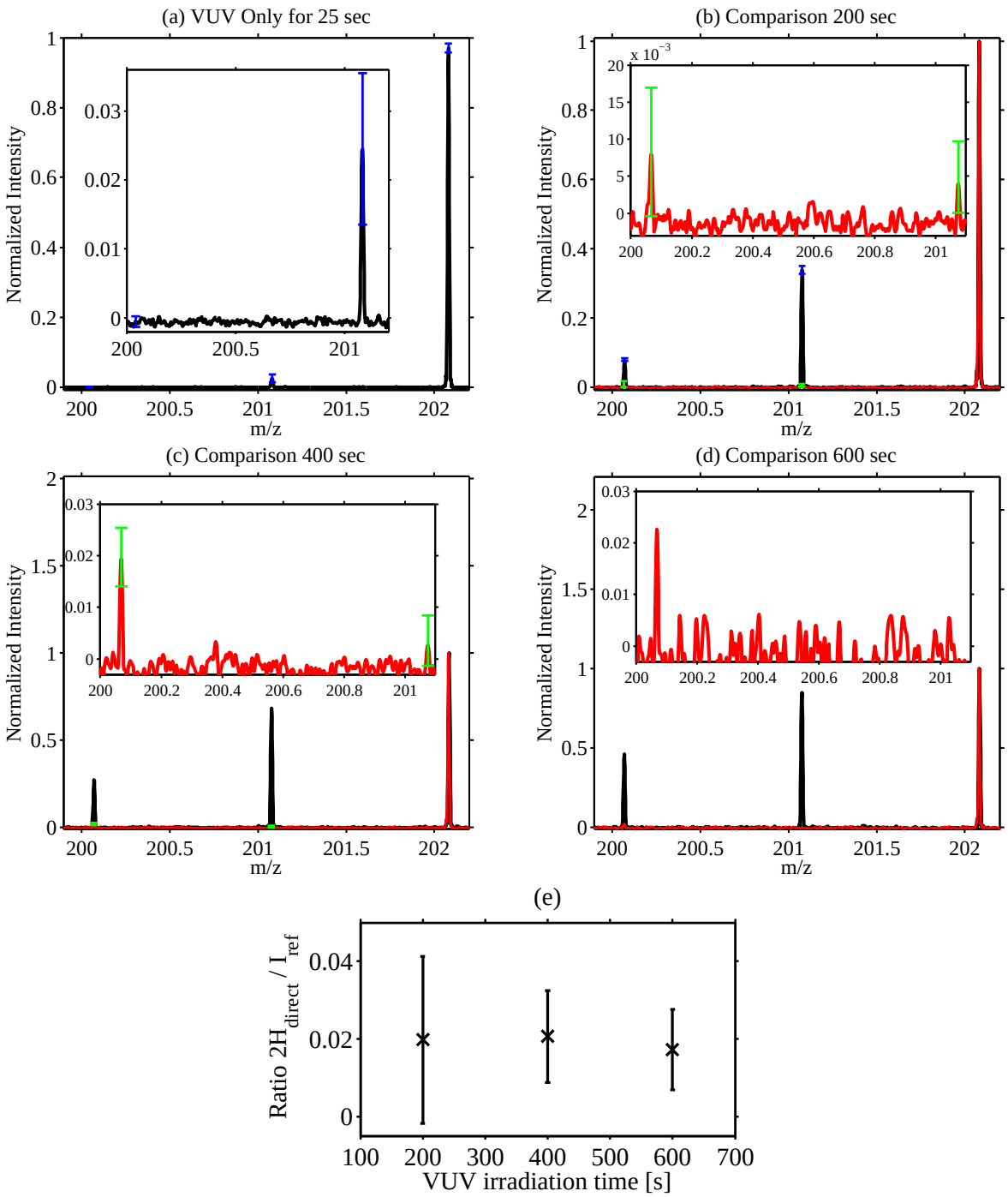

Figure S13: (a) Mass spectrum for a VUV irradiation time of 25 s. The insert is a zoom on the $[Pyr\text{-}H]^+$ and $[Pyr\text{-}2H/H_2]^+$ peaks. (b-d) Mass spectra for a VUV irradiation time of 200, 400, and 600 s respectively without $[Pyr\text{-}H]^+$ ejection (black curves) and with $[Pyr\text{-}H]^+$ ejection all 25 s (red curves). The inserts show a zoom on the $[Pyr\text{-}H]^+$ and $[Pyr\text{-}2H/H_2]^+$ peaks. (e) Ratio of the direct $2H/H_2$ loss peak to the total H and $2H/H_2$ production for the three VUV irradiation times, which leads to a value of 1.9 ± 1.4 %.

References

(S1) West, B.; Castillo, S. R.; Sit, A.; Mohamad, S.; Lowe, B.; Joblin, C.; Bodi, A.; Mayer, P. M. Unimolecular reaction energies for polycyclic aromatic hydrocarbon ions. *Phys. Chem. Chem. Phys.* **2018**, *20*, 7195–7205.

(S2) West, B.; Useli-Bacchitta, F.; Sabbah, H.; Blanchet, V.; Bodi, A.; Mayer, P. M.; Joblin, C. Photodissociation of Pyrene Cations: Structure and Energetics from $C_{16}H_{10}^{+}$ to C_{14}^{+} and Almost Everything in Between. *J. Phys. Chem. A* **2014**, *118*, 7824–7831.

(S3) Wolf, M.; Kiefer, H. V.; Langeland, J.; Andersen, L. H.; Zettergren, H.; Schmidt, H. T.; Cederquist, H.; Stockett, M. H. Photo-stability of super-hydrogenated PAHs determined by action spectroscopy experiments. *Astrophys. J.* **2016**, *832*, 24.

(S4) Marciniak, A.; Joblin, C.; Mulas, G.; Mundlapati, V. R.; Bonnamy, A. Photodissociation of aliphatic PAH derivatives under relevant astrophysical conditions. *Astron. Astrophys.* **2021**, *652*, A42.